Shear-wave Anisotropy in the Earth's Inner Core

Sheng Wang[1], Hrvoje Tkalčić[1]

[1]Research School of Earth Sciences, The Australian National University, ACT 2601, Australia.

Corresponding author:

Sheng Wang (sheng.wang@anu.edu.au), Hrvoje Tkalčić (hrvoje.tkalcic@anu.edu.au)

Key Points:

- We observe shear-wave anisotropy in the Earth's inner-core based on time and amplitude variations of earthquake coda-correlation wavefield
- Inner-core shear waves travel faster for oblique than equatorial angles relative to Earth's rotation axis by at least ~5s (~0.8% anisotropy)
- The new observations rule out one of the bcc-iron models in the inner core, although we cannot uniquely determine the dominating model

Keywords:

Earth's inner core; Shear-wave anisotropy; Iron crystal structure

Abstract

Earth's inner core anisotropy is widely used to infer the deep Earth's evolution and present dynamics. Many compressional-wave anisotropy models have been proposed based on seismological observations. In contrast, inner-core shear-wave (J-wave) anisotropy – on a par with the compressional-wave anisotropy – has been elusive. Here we present a new class of the J-wave anisotropy observations utilizing earthquake coda-correlation wavefield. We establish that the coda-correlation feature I2-J, sensitive to J-wave speed, exhibits time and amplitude changes when sampling the inner core differently. J-waves traversing the inner core near its center travel faster for the oblique than equatorial angles relative to the Earth's rotation axis by at least ~5 s. The simplest explanation is the J-wave cylindrical anisotropy with a minimum strength of ~0.8%, formed through the lattice-preferred-orientation mechanism of iron. Although we cannot uniquely determine its stable iron phase, the new observations rule out one of the body-centered-cubic iron models.

Plain Language Summary

Earth's inner core anisotropy – the directional dependence of seismic wave speed in the inner core – contains essential information of deep Earth's structure and dynamics. It results from a preferred alignment of iron crystals related to the formation and post-formation dynamics of the inner core. Many studies have investigated the inner core anisotropy observed for compressional waves. In contrast, possible anisotropy for the inner-core shear waves remains elusive. This study presents a new class of inner-core shear-wave anisotropy observations based on recent advances in earthquake coda-correlation wavefield. We find that the coda-correlation feature I2-J, sensitive to the inner-core shear-wave speed, exhibits variable timing and amplitude for sampling the inner core in different directions. Quantitatively, inner-core shear waves travel faster for at least ~5 s in directions oblique to the Earth's rotation axis than directions parallel to the equatorial plane. The simplest and most plausible explanation for our

observations is the inner-core shear-wave anisotropy with a strength of ~0.8% or higher. We can rule out at least one of the body-centered-cubic iron models in the inner core, although the other models are not distinguishable.

1 Introduction

It has been eight and a half decades since the discovery of the Earth's inner core (IC) (Lehmann, 1936). Understanding the IC structure and dynamics is of high priority to geoscientists, given its active role in the Earth's evolution (Tkalčić, 2017). This includes coupling with the liquid outer core, which sustains the geodynamo (Braginsky, 1963; Buffett et al., 1996) and possibly affects the lowermost mantle dynamics (Aubert et al., 2008; Gubbins et al., 2011), and even the processes at Earth's surface (Biggin et al., 2015). One direction in IC studies is its elastic anisotropy. The anisotropy strength and volumetric dependence may help decipher the IC evolution and its current state (Tkalčić, 2017). This is because the anisotropic properties reveal a preferred alignment of iron crystals (Stixrude & Cohen, 1995; Steinle-Neumann et al., 2001; Belonoshko et al., 2008) formed during the solidification (Karato 1993; Bergman, 1997) or post-solidification deformation progress (Jeanloz & Wenk, 1988; Yoshida et al., 1996; Wenk et al., 2000) coupled with the geodynamo (Karato, 1999; Buffett & Wenk, 2001). However, it is uncertain which type of iron crystal, hexagonal-close-packed (hcp) (Stixrude & Cohen, 1995; Steinle-Neumann et al., 2001) or body-centered-cubic (bcc) (Vočadlo et al., 2003; Belonoshko et al., 2008; Calvet & Margerin, 2008) structure, is stabilized in the IC.

Pioneering studies characterized the anisotropy based on faster compressional waves traversing the IC in directions quasi-parallel to the Earth's rotation axis than in equatorial directions (Poupinet et al., 1983; Morelli et al., 1986; Woodhouse et al., 1986; see also Shearer et al., 1988; Creager, 1992; Tromp, 1993). However, subsequent observations revealed more complex anisotropic properties of the IC (Figure 1), such as a quasi-isotropic thin layer in the upper IC (e.g., Shearer, 1994; Song & Helmberger, 1995) and a hemispherical dichotomy of the IC (e.g., Tanaka & Hamaguchi, 1997; Niu & Wen, 2001; Waszek & Deuss, 2011). Notably, the innermost part of the IC (IMIC) was found to present distinct anisotropic behavior

from the outer IC (OIC) (e.g., Ishii & Dziewoński, 2002; Beghein & Trampert, 2003; Cormier & Stroujkova, 2005; Stephenson et al., 2021). Studies in the last two decades reveal that the slowest direction of compressional-wave propagation in the IMIC is tilted relative to the Earth's rotation axis, while in the OIC, it is equatorial. But this contrast is not well constrained due to limited observations for IC central part that require source-receiver pairs close to 180°.

More observational evidence is required to reconcile these properties and the different mechanisms behind them. However, the existing observations are limited to IC compressional-wave anisotropy. Possible anisotropy for IC shear waves (J waves) that constrains the central part of the IC remains elusive. To our best knowledge, there are minimal direct observations of J waves (Julian et al., 1972; Okal & Cansi, 1998; Deuss et al., 2000; Cao et al., 2005; Wookey & Helffrich, 2008), likely because of the very weak amplitude of J waves (Shearer et al., 2011).

Here we present a new observation of IC shear-wave anisotropy based on recent advances in global coda-correlation wavefield (Phạm et al., 2018; Wang & Tkalčić, 2020; Tkalčić et al., 2020). We observe stable time and amplitude variations for the coda-correlation feature I2-J (Tkalčić & Phạm, 2018) sensitive to J-wave speed at the periods 15-50 s when its constituents sample the IC in different directions. The I2-J is formed by pairs of seismic waves (Figures 1b and 2a-c). We argue that the observed variations are due to IC shear-wave anisotropy based on analyzing and eliminating multiple possible causes. We then evaluate the J-wave anisotropy strength and examine various iron crystal models which can cause anisotropy. We show that J waves traveling in directions oblique to the Earth's rotation axis travel faster than those traveling in the equatorial plane. Although we cannot utilize J waves in planes parallel to the rotation axis

and determine whether the hcp or bcc iron model dominates the IC from our observations alone, we show that we can rule out one bcc model from many candidate models.

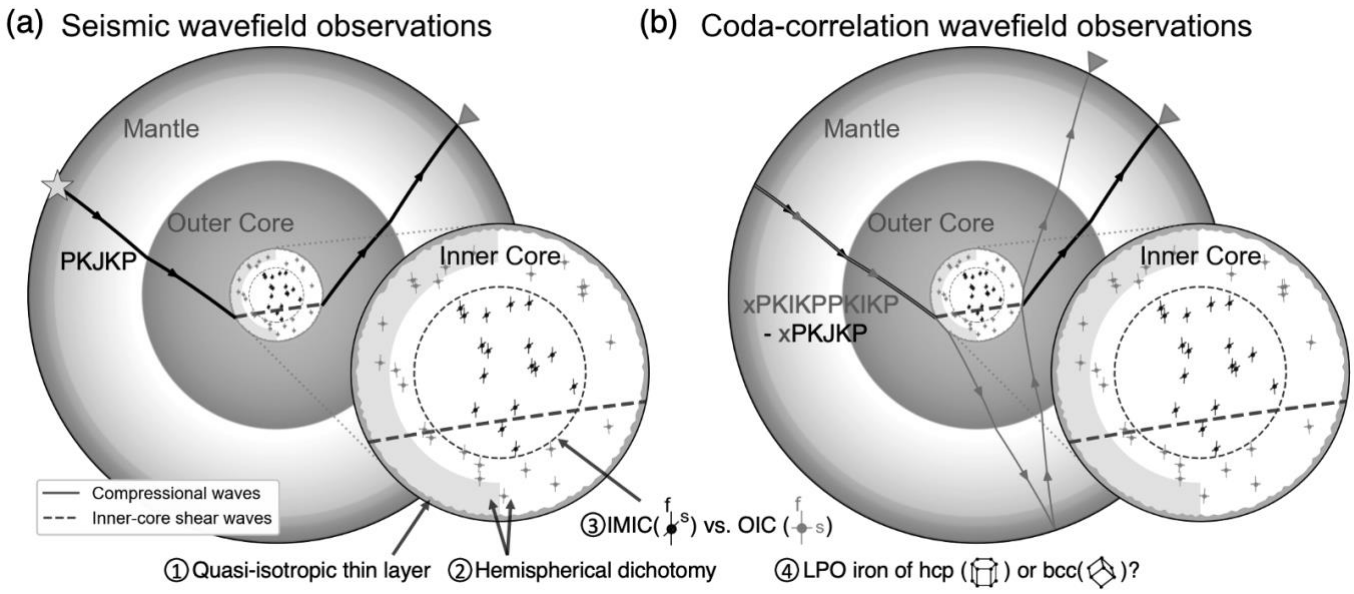

Figure 1. Complex anisotropic IC sampled by seismic wavefield and coda-correlation wavefield. The observed complexities shown in the insets are explained in the main text. (**a**) Ray path for a PKJKP wave from an event (star) to a receiver (triangle). The dashed line indicates the IC shear wave (J wave). (**b**) A diagram for correlation feature I2-J formed due to the similarity between two seismic waves: xPKIKPPKIKP (xI2) and xPKJKP (xJ) recorded at two receivers (triangles), respectively. "x" in the nomenclature represents any common combination of ray legs for the two seismic waves and is not shown. The dashed line indicates the J wave for the pair xI2-xJ. Other pairs of seismic waves contributing to I2-J and the resultant diverse J-wave directions are explained in the main text and shown in Figure 2.

2 The Observations and Confirmation of J-wave Anisotropy from Coda-correlation Wavefield

We compute earthquake coda-correlation wavefields for I2-J features following Phạm et al. (2018) and Wang and Tkalčić (2020). The I2-J is formed due to the similarity of seismic waves in a plane proximal to the great-circle plane defined by a receiver pair (Tkalčić & Phạm, 2018; Wang & Tkalčić, 2020). Multiple seismic waves can contribute to forming PKIKPPKIKP-PKJKP (I2-J) in a great-circle plane, such as xPKIKPPKIKP-xPKJKP (xI2-xJ) and xPKIKPPKIKPPKIKP-xPKJKPPKIKP (xI3-xJI) (Figures 2a-c), in which "x" represents the common ray legs for a pair of seismic waves. Therefore, we cannot

111 uniquely define the direction for an individual J-wave ray path for the feature I2-J. Accordingly, we bin
112 great-circle planes based on the angle φ for which $90° - \varphi$ is the angle between the plane's normal and
113 the Earth's rotation axis. Figures 2d-f showcase quasi-equatorial (φ~90°), oblique (φ~50°), and quasi-
114 polar (φ~0°) planes. In each of the planes, J-wave directions vary. In the quasi-equatorial plane, J-wave
115 directions are exclusively quasi-equatorial. J-wave directions can range from equatorial to oblique in the
116 oblique plane, and the more oblique the plane gets, the more versatile J-wave directions become. In the
117 quasi-polar plane, J waves can take arbitrary directions.
118
119 We then select the events with hypocenters proximal to the great-circle planes (Figures 2g-i). We
120 empirically select events close to the great-circle path for a spherical distance smaller than 15°, and
121 exclude those farther than 15° (Wang & Tkalčić, 2020). After the selection, for specific φ, the I2-J is
122 predominantly sensitive to the Earth structure proximal to the great-circle plane (Wang & Tkalčić, 2020).
123 We consider global events regardless of their epicentral distances. Any event close to the great-circle plane
124 can contribute to forming the correlation feature I2-J (Figures 2a-c). Subsequently, we compute coda-
125 correlation stacks for different φ ranges, with a step of 10° (Figure S4; see Methods section in the
126 supporting information), and we conclude that I2-J is not prominently visible in all ranges. We, therefore,
127 compute stacks for 20°-wide bins (Figures 3a-b).
128
129 As shown in Figure 3, I2-J exhibits a variation in time for different φ ranges. We find that the I2-J timing
130 for the bin φ=40°-60° (oblique planes) lags ~5 s behind the bin φ=60°-80° (quasi-equatorial planes)
131 (Figures 3a-d) via slant-stack analyses (see Methods section in the supporting information). This time
132 variation is robust given that the I2-J is a stacked cross-correlation feature based on ten-year recordings
133 for globally distributed events and receivers (Figure S1). We test the stability of time variations by

analyses with denser bins (Figures 3g-i, S6, and S7) and bootstrap experiments (Figure S8 and Methods section in the supporting information).

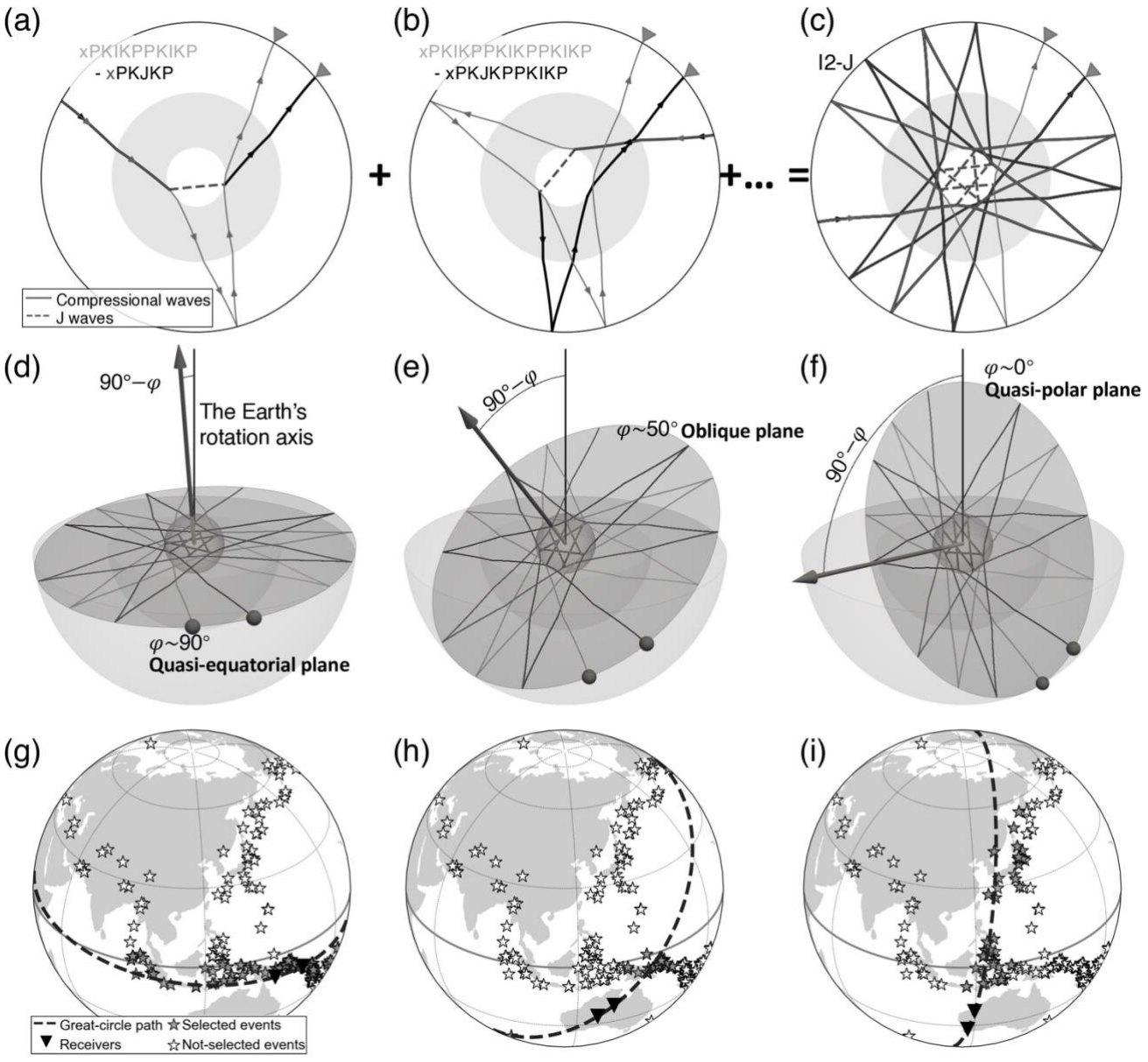

Figure 2. The ray-path geometry of the coda-correlation feature I2-J. (**a**) The I2-J can be formed by the interference between two seismic waves: xPKIKPPKIKP (xI2) and xPKJKP (xJ), recorded at two receivers (triangles), respectively. The "x" represents the common propagation legs for the two waves. The dashed line represents the IC shear waves (J waves). (**b**) The I2-J formed by another two seismic waves: xPKIKPPKIKPPKIKP (xI3) and xPKJKPPKIKP (xJI). (**c**) Combined (a), (b) plus other pairs not

shown in a) and b) (xI4-xJI2, xI5-xJI3, xI6-xJI4, xI7-xJI5) that contribute to the correlation feature I2-J. (**d**) I2-J ray paths inside a quasi-equatorial great-circle plane (φ~90°). The plane passes through two receivers (black balls). The angle between the plane's normal (black arrow) and the Earth's rotation axis is defined as $90° - \varphi$. All J-wave ray paths in the quasi-equatorial plane are in quasi-equatorial directions (relative to the Earth's rotation axis). (**e**) Same as d) but for an oblique plane (φ~50°). The J-wave ray paths exhibit a range of equatorial and oblique directions relative to the Earth's rotation axis. (**f**) Same as d) but for a quasi-polar plane (φ~0°). The J-wave ray paths are in arbitrary directions relative to the Earth's rotation axis. (**g**) An example showing a selection of events (stars) for a quasi-equatorial great-circle plane for two receivers (black triangles). We select events within the spherical distance of 15° to the great-circle path and exclude those farther than 15°. (**h, i**) Similar to (g) but for oblique and quasi-polar planes, respectively.

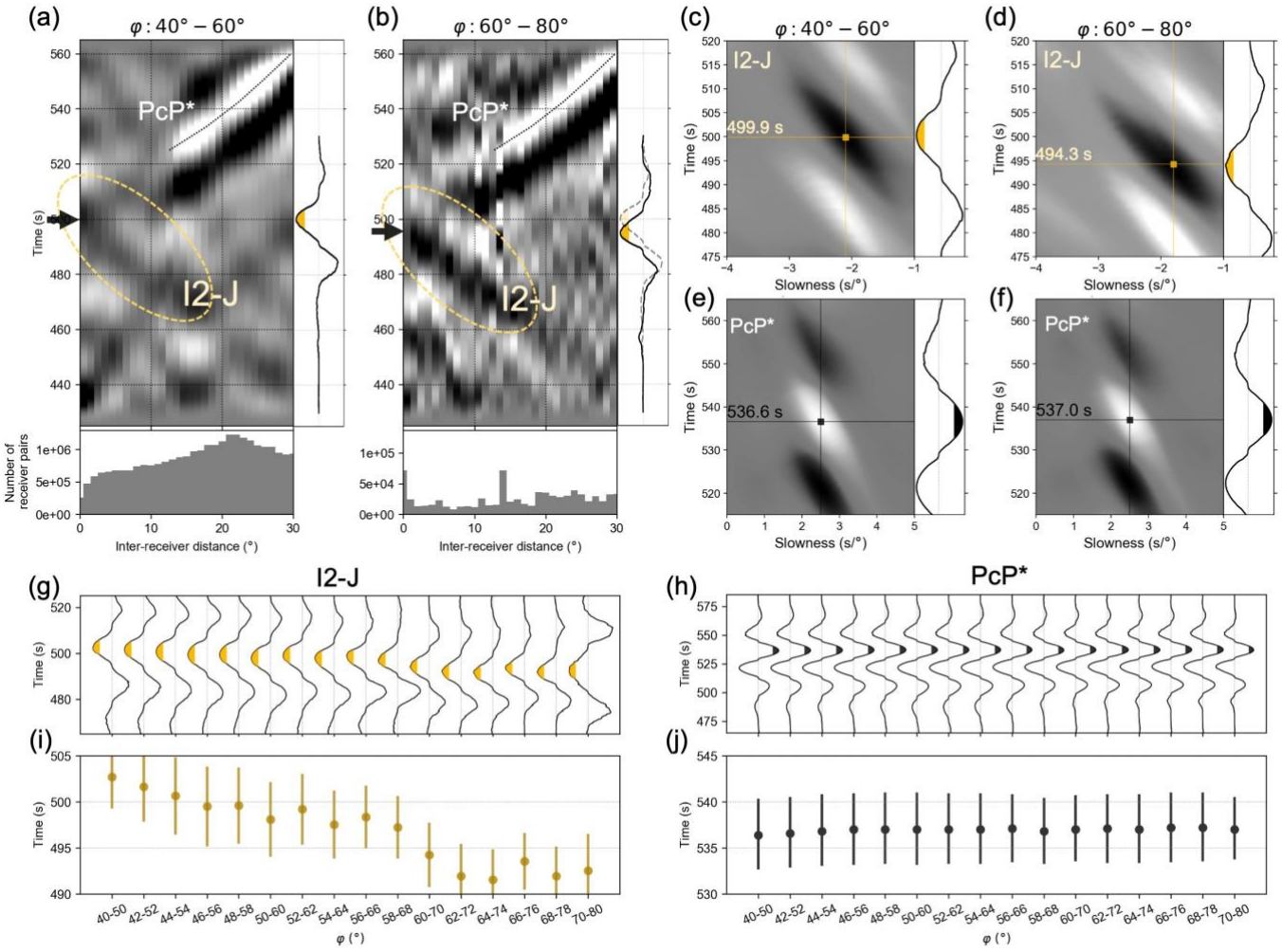

Figure 3. Observations of IC shear-wave anisotropy in coda-correlation wavefield. (**a, b**) Coda-correlograms and frequency histograms of receiver pairs in different inter-receiver distance bins for two φ ranges: (a) 40°-60°, (b) 60°-80°. φ is defined in Figure 2; yellow ellipses and black arrows indicate the coda-correlation feature I2-J sensitive to the IC shear-wave speed; dotted lines indicate the feature PcP*. Positive correlation amplitudes are in white shades, and negative are in black shades; the intensity of the black or white indicates the amplitude strength. The I2-J waveform stacks are shown alongside the correlograms. (**c, d**) Slant stacks of I2-J for the two different φ ranges, 40°-60°, and 60°-80°, respectively. The yellow dots correspond to the lower branch of the I2-J cusp. Each slant stack is normalized with respect to the maximal amplitude. The I2-J waveform stacks are shown alongside the slant stacks. (**e, f**) Similar to (c, d) but for PcP*. (**g, h**) I2-J and PcP* waveform stacks based on slant stacks for different φ ranges. Colored areas correspond to stack amplitudes greater than 80% of the maximum. (**i, j**) Time measurements of the I2-J and PcP* waveform stacks. Dots correspond to the stacks' maximum amplitudes. Vertical bars correspond to the time range of the colored area in (g, h).

To explain the time variation, we consider multiple possibilities, similar in the scope to analyses of IC compressional-wave travel times (e.g., Poupinet et al., 1983; Morelli et al., 1986; Shearer et al., 1988; Creager, 1992). The possible explanations for our observations are 1) mantle structure, core-mantle-boundary (CMB) topography, and ellipticity of the Earth, 2) outer-core (OC) heterogeneity, 3) IC heterogeneity, 4) IC compressional-wave anisotropy, and 5) IC shear-wave anisotropy. In short, these considerations show that the shear-wave anisotropy is the simplest and most likely cause for the observed travel time variations.

Considering the first cause, the correlation stacks for each φ range correspond to a laterally-averaged mantle due to the mixture of raypaths at diverse directions (Figure 2). Hence, the signature from mantle heterogeneity, CMB topography, and Earth's ellipticity is averaged out. This is evident via the correlation feature PcP*, sensitive to the mantle structure, CMB topography, and Earth's ellipticity. Namely, for different φ, PcP* is nearly invariant compared to I2-J (Figures 3g-j), that the measured time variation for

PcP* is less than 0.5 s (Figures 3e-f). In conclusion, mantle structure, CMB topography, or Earth's ellipticity cannot reconcile such a difference between I2-J and PcP*.

As far as the OC heterogeneity is considered, effects due to possible OC structure are mitigated due to the diverse I2-J ray paths in the OC (Figure 2). Notably, the bulk of the OC is well-mixed and homogeneous due to vigorous convection (Stevenson, 1987). Romanowicz et al. (2003) showed that OC tangent-cylinder structure could explain PKP observations, although this was later disputed (e.g., Souriau et al., 2003; Ishii and Dziewoński, 2005). Therefore, the possibility of a complex structure in the OC affecting I2-J is even smaller than 1) to explain the I2-J variations.

IC heterogeneity requires significant structural anomalies in the bulk of the IC. If such anomaly distribution indeed exists, there should also be evidence in compressional-wave travel time observations. However, that has not been observed for the bulk of the IC (Shearer, 1994). The observed lateral variation in travel times for the waves sampling the upper parts of the IC (Tanaka & Hamaguchi, 1997; Niu & Wen, 2001; Yee et al., 2014) is not sufficiently large to explain our observations. In conclusion, IC heterogeneity would have to be more complex than the IC shear-wave anisotropy.

The IC has been hypothesized to be cylindrically anisotropic for compressional waves based on seismic travel times (Morelli et al., 1986; Shearer et al., 1988; Creager, 1992) and normal modes (Woodhouse et al., 1986; Tromp, 1993). PKIKP waves propagate faster along the rotation axis than along equatorial directions. However, the IC compressional-wave anisotropy cannot explain the observed time difference for I2-J. The IC compression waves (I-wave legs) contributing to I2-J do not penetrate deep into IC. The I waves sample the topmost IC at a maximal depth less than 10 km below the IC boundary (ICB) (Figure S11), and the total travel time for the I legs is less than 50 s. Therefore, if the IC compressional-wave

anisotropy were the cause for our observations, it would have to be at least 10% in the topmost 10 km of the IC, which has not been observed. Quite to the contrary, a thin layer in the upper IC is revealed to be quasi-isotropic (e.g., Shearer, 1994; Song & Helmberger, 1995).

The IC can be anisotropy for shear waves due to lattice-preferred orientation (LPO) of iron crystal in either hcp (Steinle-Neumann et al., 2001; Stixrude & Cohen, 1995) or bcc (Belonoshko et al., 2008; Calvet & Margerin, 2008; Vočadlo et al., 2003) models in the IC hypothesized for explaining the compressional-wave anisotropy. By invoking these models, theoretical computations predict travel-time difference up to a few tens of seconds for J waves sampling the whole bulk of the IC in different directions (Song, 1997; Stixrude & Cohen, 1995; Vočadlo et al., 2009). That is sufficient to explain the observed ~5 s time difference via invoking a portion of LPO of iron inside the IC. The J-wave anisotropy might be different in the OIC and the IMIC because the same is true for the P-wave anisotropy (e.g., Ishii & Dziewoński, 2002; Beghein & Trampert, 2003; Cormier & Stroujkova, 2005; Stephenson et al., 2021). However, from the observations of I2-J, we cannot distinguish between the OIC and the IMIC. As shown in Figure S11, the J waves contributing to I2-J sample the bulk of the IC from the ICB to depth ~815 km below the ICB, and that is similar for all I2-J at different inter-receiver distances. Therefore, the observed ~5 s time difference for I2-J corresponds to an aggregated J-wave anisotropy for the whole bulk of the IC.

J-wave anisotropy is also supported by the varied strength of the I2-J cusp for different angle φ ranges. The I2-J cusp presents weaker amplitude for φ in the range 40°-60° than in 60°-80° (Figures 3a-b), and loses its visibility when φ approaches 0° although there are still a large number of cross-correlation pairs (Figure S4). When φ is close to 0°, the J waves contributing to I2-J sample the IC at varying angles relative to the Earth's rotation axis (Figure 2f) and hence have notable different travel times due to anisotropy.

Namely, the time difference due to shear-wave anisotropy can be up to tens of seconds, as predicted (Song, 1997; Stixrude & Cohen, 1995; Vočadlo et al., 2009). The time difference between J waves can decrease the amplitude of their stacks when forming I2-J (Wang & Tkalčić, 2020). To test the effect of anisotropy on the strength of I2-J, we perform a synthetic experiment (see Methods section in the supporting information). As shown in Figure S10, J waves interfere destructively for polar and polar-oblique planes, yielding a decrease in the amplitude of I2-J stacks. The observations confirm that.

In contrast, since all J waves have sufficiently similar travel times for the equatorial and quasi-equatorial planes, they constructively interfere to form a clear I2-J feature. That is evident by the strong I2-J amplitude for φ in 60°-80° although the number of receiver pairs is less than one-tenth of those at other φ ranges (Figures 3a-b and S4). We cannot rule out attenuation anisotropy in the IC (Mäkinen et al., 2014; Souriau & Romanowicz, 1996), which would also contribute to explaining the unclear I2-J feature. Strong attenuation in polar directions would weaken a portion of J waves constituting I2-J for φ close to 0°. But for φ close to 90°, the constituents of I2-J do not suffer from the strong attenuation effects, and their stacks result in visible I2-J features.

3 The Anisotropy Strength and Implications for the Stable Phase of Iron and Viscosity

Based on the above rationale, we evaluate the IC shear-wave cylindrical anisotropy strength by defining the angle ξ as the angle between the individual J-wave raypath and the Earth's rotation axis (Figure 4a; Shearer et al., 1988; Tkalčić, 2015). For I2-J in a plane defined by φ, the angles ξ of contributing J waves are distributed in the interval from φ to 90° (Figure 2). The observed I2-J travel time corresponds to an averaged J wave at those different ξ angles. We evaluate that the J waves are faster for at least ~5 s at the oblique angles (ξ=40°-60°) than at the equatorial angles (ξ=60°-80°) (see Methods section in the

supporting information). The ~5 s time difference sets a minimum bound of shear-wave anisotropy strength to ~0.8%. We do not have enough resolution for polar angles due to the unclear I2-J when φ approaches 0° (Figure S4). The ~0.8% J-wave anisotropy is comparable to the ~1% based on direct seismic body wave observations (Wookey & Helffrich, 2008).

Unlike some other coda-correlation features (e.g., I2* in Wang & Tkalčić (2020)), I2-J cannot be separated into unambiguous (timing-wise) constituents (Wang & Tkalčić, 2020). Hence, we cannot determine the travel times of individual J waves along different raypaths. This prevents us from observing J-wave splitting into two polarized shear waves (quasi-SV and quasi-SH) propagating at different speeds. Furthermore, the quasi-SH in the IC can be relatively weaker than the quasi-SV because of its ineffective conversion from and to the P waves at the ICB. Nevertheless, the J-wave observations derived from coda-correlation stacks correspond to an average of two split shear waves.

Various crystalographic models have been suggested to explain the cylindrical anisotropy of the IC based on compressional-wave observations, as summarized in many studies (e.g., Mattesini et al., 2010; Romanowicz et al., 2016; Vočadlo et al., 2009). Although we cannot obtain an evaluation for J-wave anisotropy based on the full range of angles ξ, we can check each model's compatibility with our observations. We consider the following models: hcp with its *c* axis quasi-parallel to the Earth's rotation axis (Figure 4a) and bcc with different crystal alignments (bcc001, bcc110, and bcc111, shown in Figures 4b-d). We calculate averaged J-wave velocities by assuming a single crystal for the whole IC (see Methods section in the supporting information). As shown in Figure 4e, the bcc001 model predicts slower J waves at oblique (ξ=40°-60°) than equatorial directions (ξ=60°-90°). That is the opposite of our observation. In contrast, the hcp, bcc110, and bcc111 models predict faster J waves at oblique than equatorial directions,

in agreement with our observation. Therefore, bcc001 can be excluded from candidate IC iron models. However, we cannot distinguish between the hcp, bcc110, and bcc111 models because they give similar travel time curves (Figure 4e). This is somewhat similar to the conclusion drawn based on direct body wave observations at shorter periods (Wookey & Helffrich, 2008), in which different models yield similar J-wave anisotropy. Both this study and Wookey & Helffrich (2008) rely on theoretical computations of elasticity for iron crystals. Wookey & Helffrich (2008) prefers an hcp model with its *c* axis perpendicular to the Earth's rotation axis considering the fastest P-waves at directions perpendicular to the *c* axis (Steinle-Neumann et al., 2001), however opposite anisotropic properties for the hcp iron were reported by different studies, related to temperature and pressure uncertainty (e.g., Antonangeli et al., 2006; Stixrude & Cohen, 1995; Vočadlo et al., 2009).

Furthermore, the predictions for single crystals exhibit much stronger anisotropy than the observations. A portion of the iron crystal's LPO, related to crystal defects or grain boundaries, could decrease the anisotropy strength. We set a model for imperfect crystal alignment (bcc111-G in Figure 4e). We set a Gaussian distribution of the cubic main diagonal orientations around the Earth's rotation axis, and the Gaussian distribution has its half maximum at 30°. This imperfect crystal alignment reduces the anisotropy strength from 25.1% (bcc111) to 10.8% (bcc111-G). The crystal imperfections are also suggested to be a reason for the lower rigidity of the IC in observations than in experimental predictions (Belonoshko et al., 2007).

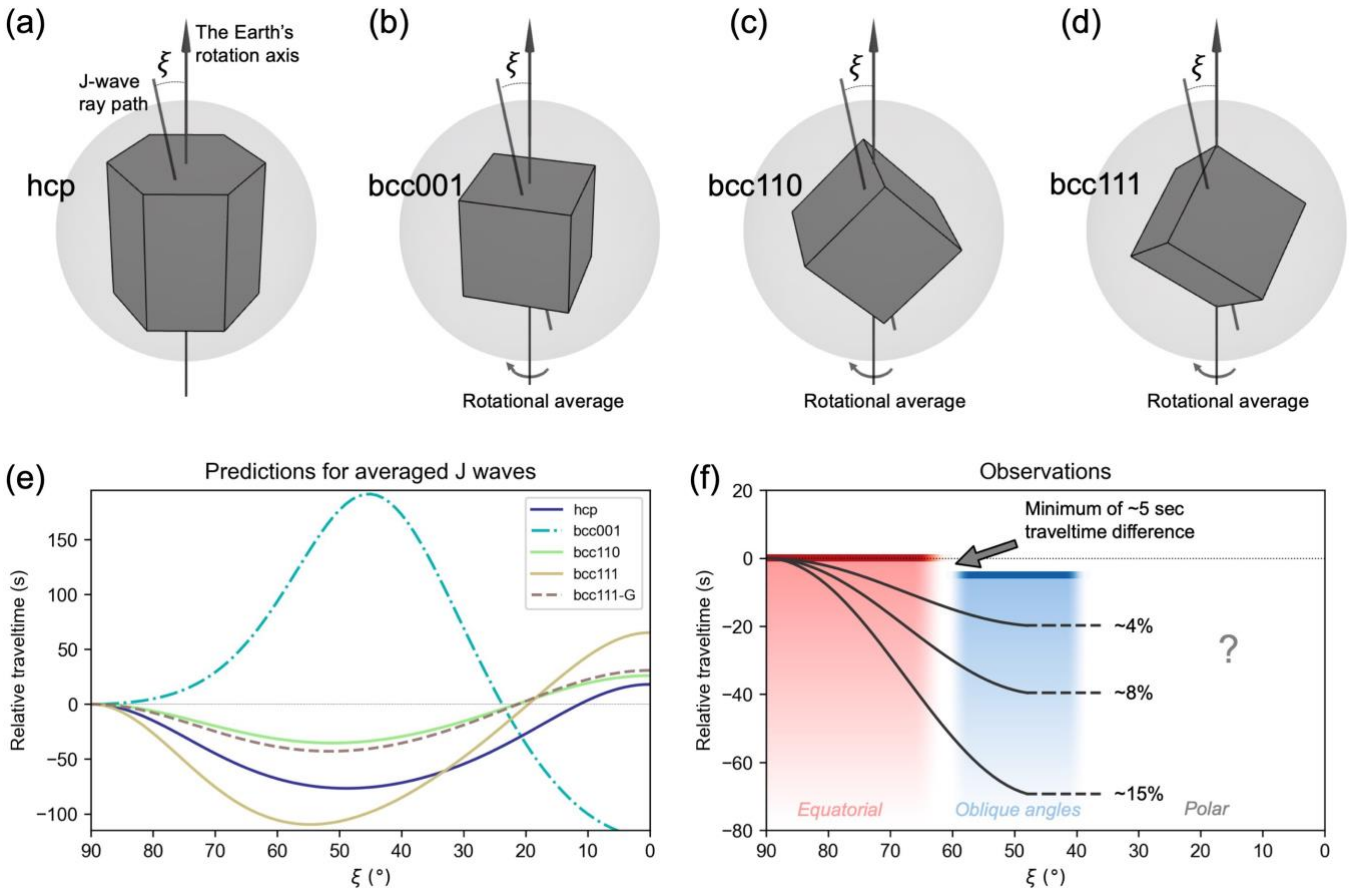

Figure 4. Hcp and bcc models for IC shear-wave anisotropy. (**a-d**) Diagrams of hcp and bcc models for iron crystal in the IC. ξ is the angle between J-wave ray paths and the Earth's rotation axis. The hcp model has its *c* axis parallel to the Earth's rotation axis. The bcc001, bcc110, and bcc111 have the cube edge, face diagonal, and main diagonal parallel to the rotation axis, respectively. (**e**) J-wave travel time predictions as a function of the angle ξ for the models shown in (a-d). bcc111-G corresponds to an imperfect crystal alignment for bcc111 (see main text). Elastic properties for different models are listed in Table S1. (**f**) Illustration of the observed relative travel times in this study. The curves indicate shear-wave anisotropy models of different strengths.

The analyses above are based on the J-wave speed variation between oblique and equatorial directions. We lack constraints in polar directions due to unclear I2-J in polar planes (φ close to 0°). In polar planes, J waves contributing to I2-J sample the IC at varying angles (ξ=0°-90°) and thus have highly variable travel times due to cylindrical anisotropy, which decreases I2-J amplitude via non-constructive stacking

(Wang & Tkalčić, 2020). A more complex asymmetric IC model departing from the cylindrical anisotropy (Romanowicz et al., 1996) can increase travel time variability and further decrease the amplitude of I2-J. The anisotropy asymmetry may imply a slow translation in addition to the preferential equatorial growth of the IC (Romanowicz et al., 1996; Frost et al., 2021). Currently, the coda-correlation observations cannot provide constraints on some proposed complex models, but they do not rule out models of asymmetric anisotropy and large-scale low-order convection in the IC (Romanowicz et al., 1996; Frost et al., 2021). A delicate grouping of I2-J with respect to longitude may shed light on the asymmetric anisotropy; however, care should be taken due to the unequal distribution of great-circle planes as a function of longitude (Figure S3).

The IC shear-wave anisotropy can bias estimation of the attenuation structure, which is an essential parameter in understanding the viscosity and the related mineral physics and dynamics of the IC (Souriau & Romanowicz, 1996; Tkalčić & Phạm, 2018). For example, the attenuation strength can be overestimated from the coda-correlation wavefield observations if anisotropy is not considered, as noted by Tkalčić & Phạm (2018). The amplitude of a correlation feature can decrease due to the stacking contributions affected by anisotropic travel times (Wang & Tkalčić, 2020). As shown in a synthetic experiment (Figure S10), the anisotropy for a simple hcp model in the IC can result in amplitude reduction >80% for I2-J stacks from φ=85° to φ=5° without adding any attenuation effect.

4 Conclusion

We observe travel time and amplitude variations for coda-correlation feature I2-J, which confirms the existence of shear-wave anisotropy in the bulk of the IC. The shear waves traverse the IC near its center faster in directions oblique to the Earth's rotation axis than in the equatorial directions. The observed travel

time difference is ~5 s, which translates to the apparent anisotropy strength of ~0.8%. However, given the increasing versatility in J-wave raypath directions for the planes progressing from equatorial to polar angles, we cannot utilize the quasi-polar planes, and 0.8% is the lower estimate of the anisotropy strength. The anisotropy can be explained by invoking a portion of LPO of iron either in hcp or bcc structure. Currently, our observations rule out the bcc001 structure, but other iron structures are not distinguishable. A delicate grouping of coda-correlation stacks may help reveal a complex IC anisotropy. Further proliferation of seismographs worldwide, including the ocean floor, will provide uniform coverage of coda-correlation observations and resolve trade-offs between anisotropic and attenuative structures.

Acknowledgments

We are grateful to Dr. Phạm Thanh-Son and other Global Seismology group members at The Australian National University for valuable discussions. We are also thankful to Prof. Maurizio Mattesini for advising us on computations of anisotropic speeds for various iron crystal models. Seismic waveform data used in this study are retrieved from IRIS DMC (https://ds.iris.edu/ds/nodes/dmc/data/) with ObspyDMT (Hosseini & Sigloch, 2017). The computations are performed at the National Computation Infrastructure (NCI Australia) computer cluster as part of the ANUMAS grant #em78. The Australian Government provides the NCI infrastructure through its National Collaborative Research Infrastructure Strategy (NCRIS). The authors declare no competing interests.

References

Antonangeli, D., Merkel, S., & Farber, D. L. (2006). Elastic anisotropy in hcp metals at high pressure and the sound wave anisotropy of the Earth's inner core. *Geophysical Research Letters*, *33*(24). https://doi.org/10.1029/2006GL028237

Aubert, J., Amit, H., Hulot, G., & Olson, P. (2008). Thermochemical flows couple the Earth's inner core growth to mantle heterogeneity. *Nature*, *454*(7205), 758–761. https://doi.org/10.1038/nature07109

Auld, B. A. (1990). *Acoustic fields and waves in solids. Vol. 1 Vol. 1*. Malabar: Krieger Publishing Company.

Beghein, C., & Trampert, J. (2003). Robust Normal Mode Constraints on Inner-Core Anisotropy from Model Space Search. *Science*, *299*(5606), 552–555. https://doi.org/10.1126/science.1078159

Belonoshko, A. B., Skorodumova, N. V., Davis, S., Osiptsov, A. N., Rosengren, A., & Johansson, B. (2007). Origin of the Low Rigidity of the Earth's Inner Core. *Science*, *316*(5831), 1603–1605. https://doi.org/10.1126/science.1141374

Belonoshko, A. B., Skorodumova, N. V., Rosengren, A., & Johansson, B. (2008). Elastic Anisotropy of Earth's Inner Core. *Science*, *319*(5864), 797–800. https://doi.org/10.1126/science.1150302

Bergman, M. I. (1997). Measurements of electric anisotropy due to solidification texturing and the implications for the Earth's inner core. *Nature*, *389*(6646), 60–63. https://doi.org/10.1038/37962

Biggin, A. J., Piispa, E. J., Pesonen, L. J., Holme, R., Paterson, G. A., Veikkolainen, T., & Tauxe, L. (2015). Palaeomagnetic field intensity variations suggest Mesoproterozoic inner-core nucleation. *Nature*, *526*(7572), 245–248. https://doi.org/10.1038/nature15523

Braginsky, S. I. (1963). Structure of the F layer and reasons for convection in the Earth's core. *Soviet Phys. Dokl.*, *149*, 8–10.

Buffett, B. A., & Wenk, H.-R. (2001). Texturing of the Earth's inner core by Maxwell stresses. *Nature*, *413*(6851), 60–63. https://doi.org/10.1038/35092543

Buffett, Bruce A., Huppert, H. E., Lister, J. R., & Woods, A. W. (1996). On the thermal evolution of the Earth's core. *Journal of Geophysical Research: Solid Earth*, *101*(B4), 7989–8006. https://doi.org/10.1029/95JB03539

Cao, A. (2005). An Observation of PKJKP: Inferences on Inner Core Shear Properties. *Science*, *308*(5727), 1453–1455. https://doi.org/10.1126/science.1109134

Calvet, M., & Margerin, L. (2008). Constraints on grain size and stable iron phases in the uppermost inner core from multiple scattering modeling of seismic velocity and attenuation. *Earth and Planetary Science Letters*, *267*(1), 200–212. https://doi.org/10.1016/j.epsl.2007.11.048

Chapman, C. H. (1981). Generalized Radon transforms and slant stacks. *Geophysical Journal International*, *66*(2), 445–453. https://doi.org/10.1111/j.1365-246X.1981.tb05966.x

Cormier, V. F., & Stroujkova, A. (2005). Waveform search for the innermost inner core. *Earth and Planetary Science Letters*, *236*(1), 96–105. https://doi.org/10.1016/j.epsl.2005.05.016

Creager, K. C. (1992). Anisotropy of the inner core from differential travel times of the phases PKP and PKIKP. *Nature*, *356*(6367), 309–314. https://doi.org/10.1038/356309a0

Deuss, A., Woodhouse, J. H., Paulssen, H., & Trampert, J. (2000). The observation of inner core shear waves. *Geophysical Journal International*, *142*(1), 67–73. https://doi.org/10.1046/j.1365-246x.2000.00147.x

Frost, D. A., Lasbleis, M., Chandler, B., & Romanowicz, B. (2021). Dynamic history of the inner core constrained by seismic anisotropy. *Nature Geoscience*, 1–5. https://doi.org/10.1038/s41561-021-00761-w

403 Gubbins, D., Sreenivasan, B., Mound, J., & Rost, S. (2011). Melting of the Earth's inner core. *Nature*,
404 *473*(7347), 361–363. https://doi.org/10.1038/nature10068
405 Hosseini, K., & Sigloch, K. (2017). ObspyDMT: a Python toolbox for retrieving and processing large
406 seismological data sets. *Solid Earth*, *8*(5), 1047–1070. https://doi.org/10.5194/se-8-1047-2017
407 Ishii, M., & Dziewoński, A. M. (2002). The innermost inner core of the earth: Evidence for a change in
408 anisotropic behavior at the radius of about 300 km. *Proceedings of the National Academy of*
409 *Sciences*, *99*(22), 14026–14030. https://doi.org/10.1073/pnas.172508499
410 Ishii, M., & Dziewoński, A. M. (2005). Constraints on the outer-core tangent cylinder using normal-
411 mode splitting measurements. *Geophysical Journal International*, *162*(3), 787–792.
412 https://doi.org/10.1111/j.1365-246X.2005.02587.x
413 Jeanloz, R., & Wenk, H.-R. (1988). Convection and anisotropy of the inner core. *Geophysical Research*
414 *Letters*, *15*(1), 72–75. https://doi.org/10.1029/GL015i001p00072
415 Julian, B. R., Davies, D., & Sheppard, R. M. (1972). PKJKP. *Nature*, *235*(5337), 317–318.
416 https://doi.org/10.1038/235317a0
417 Karato, S. (1993). Inner Core Anisotropy Due to the Magnetic Field—induced Preferred Orientation of
418 Iron. *Science*, *262*(5140), 1708–1711. https://doi.org/10.1126/science.262.5140.1708
419 Karato, S. (1999). Seismic anisotropy of the Earth's inner core resulting from flow induced by Maxwell
420 stresses. *Nature*, *402*(6764), 871–873. https://doi.org/10.1038/47235
421 Kennett, B. L. N., Engdahl, E. R., & Buland, R. (1995). Constraints on seismic velocities in the Earth
422 from traveltimes. *Geophysical Journal International*, *122*(1), 108–124.
423 https://doi.org/10.1111/j.1365-246X.1995.tb03540.x
424 Lehmann, I. (1936). P'. *Publications Du Bureau CentralSeismologique International, Série A, Travaux*
425 *Scientifique*, *14*, 87–115.

426 Lin, J.-F., Mao, Z., Yavaş, H., Zhao, J., & Dubrovinsky, L. (2010). Shear wave anisotropy of textured
427 hcp-Fe in the Earth's inner core. *Earth and Planetary Science Letters*, *298*(3), 361–366.
428 https://doi.org/10.1016/j.epsl.2010.08.006
429 Mäkinen, A. M., Deuss, A., & Redfern, S. A. T. (2014). Anisotropy of Earth's inner core intrinsic
430 attenuation from seismic normal mode models. *Earth and Planetary Science Letters*, *404*, 354–
431 364. https://doi.org/10.1016/j.epsl.2014.08.009
432 Mao, W. L., Struzhkin, V. V., Baron, A. Q. R., Tsutsui, S., Tommaseo, C. E., Wenk, H.-R., et al. (2008).
433 Experimental determination of the elasticity of iron at high pressure. *Journal of Geophysical*
434 *Research: Solid Earth*, *113*(B9). https://doi.org/10.1029/2007JB005229
435 Mattesini, M., Belonoshko, A. B., Buforn, E., Ramírez, M., Simak, S. I., Udías, A., et al. (2010).
436 Hemispherical anisotropic patterns of the Earth's inner core. *Proceedings of the National*
437 *Academy of Sciences*, *107*(21), 9507–9512. https://doi.org/10.1073/pnas.1004856107
438 Morelli, A., Dziewonski, A. M., & Woodhouse, J. H. (1986). Anisotropy of the inner core inferred from
439 PKIKP travel times. *Geophysical Research Letters*, *13*(13), 1545–1548.
440 https://doi.org/10.1029/GL013i013p01545
441 Niu, F., & Wen, L. (2001). Hemispherical variations in seismic velocity at the top of the Earth's inner
442 core. *Nature*, *410*(6832), 1081–1084. https://doi.org/10.1038/35074073
443 Okal, E. A., & Cansi, Y. (1998). Detection of PKJKP at intermediate periods by progressive multi-
444 channel correlation. *Earth and Planetary Science Letters*, *164*(1), 23–30.
445 https://doi.org/10.1016/S0012-821X(98)00210-6
446 Phạm, T.-S., Tkalčić, H., Sambridge, M., & Kennett, B. L. N. (2018). Earth's Correlation Wavefield:
447 Late Coda Correlation. *Geophysical Research Letters*, *45*(7), 3035–3042.
448 https://doi.org/10.1002/2018GL077244

449 Poupinet, G., Pillet, R., & Souriau, A. (1983). Possible heterogeneity of the Earth's core deduced from
450 PKIKP travel times. *Nature*, *305*(5931), 204–206. https://doi.org/10.1038/305204a0
451 Romanowicz, B., Li, X.-D., & Durek, J. (1996). Anisotropy in the Inner Core: Could It Be Due To Low-
452 Order Convection? *Science*, *274*(5289), 963–966. https://doi.org/10.1126/science.274.5289.963
453 Romanowicz, B., Tkalčić, H., & Bréger, L. (2003). On the origin of complexity in PKP travel time data.
454 In V. Dehant, K. C. Creager, S. Karato, & S. Zatman (Eds.), *Geodynamics Series* (Vol. 31, pp.
455 31–44). Washington, D. C.: American Geophysical Union. https://doi.org/10.1029/GD031p0031
456 Romanowicz, B., Cao, A., Godwal, B., Wenk, R., Ventosa, S., & Jeanloz, R. (2016). Seismic anisotropy
457 in the Earth's innermost inner core: Testing structural models against mineral physics
458 predictions. *Geophysical Research Letters*, *43*(1), 93–100.
459 https://doi.org/10.1002/2015GL066734
460 Shearer, P. M. (1994). Constraints on inner core anisotropy from PKP(DF) travel times. *Journal of*
461 *Geophysical Research: Solid Earth*, *99*(B10), 19647–19659. https://doi.org/10.1029/94JB01470
462 Shearer, P. M., Toy, K. M., & Orcutt, J. A. (1988). Axi-symmetric Earth models and inner-core
463 anisotropy. *Nature*, *333*(6170), 228–232. https://doi.org/10.1038/333228a0
464 Shearer, P. M., Rychert, C. A., & Liu, Q. (2011). On the visibility of the inner-core shear wave phase
465 PKJKP at long periods. *Geophysical Journal International*, *185*(3), 1379–1383.
466 https://doi.org/10.1111/j.1365-246X.2011.05011.x
467 Song, X. (1997). Anisotropy of the Earth's inner core. *Reviews of Geophysics*, *35*(3), 297–313.
468 https://doi.org/10.1029/97RG01285
469 Song, X., & Helmberger, D. V. (1995). Depth dependence of anisotropy of Earth's inner core. *Journal*
470 *of Geophysical Research: Solid Earth*, *100*(B6), 9805–9816. https://doi.org/10.1029/95JB00244

471 Souriau, A., & Romanowicz, B. (1996). Anisotropy in inner core attenuation: A new type of data to
472 constrain the nature of the solid core. *Geophysical Research Letters*, *23*(1), 1–4.
473 https://doi.org/10.1029/95GL03583
474 Souriau, A., Teste, A., & Chevrot, S. (2003). Is there any structure inside the liquid outer core?
475 *Geophysical Research Letters*, *30*(11). https://doi.org/10.1029/2003GL017008
476 Steinle-Neumann, G., Stixrude, L., Cohen, R. E., & Gülseren, O. (2001). Elasticity of iron at the
477 temperature of the Earth's inner core. *Nature*, *413*(6851), 57–60.
478 https://doi.org/10.1038/35092536
479 Stephenson, J., Tkalčić, H., & Sambridge, M. (2021). Evidence for the Innermost Inner Core: Robust
480 Parameter Search for Radially Varying Anisotropy Using the Neighborhood Algorithm. *Journal*
481 *of Geophysical Research: Solid Earth*, *126*(1), e2020JB020545.
482 https://doi.org/10.1029/2020JB020545
483 Stevenson, D. J. (1987). Limits on lateral density and velocity variations in the Earth's outer core.
484 *Geophysical Journal International*, *88*(1), 311–319. https://doi.org/10.1111/j.1365-
485 246X.1987.tb01383.x
486 Stixrude, L., & Cohen, R. E. (1995). High-Pressure Elasticity of Iron and Anisotropy of Earth's Inner
487 Core. *Science*, *267*(5206), 1972–1975. https://doi.org/10.1126/science.267.5206.1972
488 Tanaka, S., & Hamaguchi, H. (1997). Degree one heterogeneity and hemispherical variation of
489 anisotropy in the inner core from PKP(BC)–PKP(DF) times. *Journal of Geophysical Research:*
490 *Solid Earth*, *102*(B2), 2925–2938. https://doi.org/10.1029/96JB03187
491 Tkalčić, H. (2015). Complex inner core of the Earth: The last frontier of global seismology. *Reviews of*
492 *Geophysics*, *53*(1), 59–94. https://doi.org/10.1002/2014RG000469

493 Tkalčić, H. (2017). *The earth's inner core: revealed by observational seismology*. Cambridge ; New
494 York, NY: Cambridge University Press.
495 Tkalčić, H., & Phạm, T.-S. (2018). Shear properties of Earth's inner core constrained by a detection of J
496 waves in global correlation wavefield. *Science*, *362*(6412), 329–332.
497 https://doi.org/10.1126/science.aau7649
498 Tkalčić, H., Phạm, T.-S., & Wang, S. (2020). The Earth's coda correlation wavefield: Rise of the new
499 paradigm and recent advances. *Earth-Science Reviews*, *208*, 103285.
500 https://doi.org/10.1016/j.earscirev.2020.103285
501 Tromp, J. (1993). Support for anisotropy of the Earth's inner core from free oscillations. *Nature*,
502 *366*(6456), 678–681. https://doi.org/10.1038/366678a0
503 Vočadlo, L., Alfè, D., Gillan, M. J., Wood, I. G., Brodholt, J. P., & Price, G. D. (2003). Possible thermal
504 and chemical stabilization of body-centred-cubic iron in the Earth's core. *Nature*, *424*(6948),
505 536–539. https://doi.org/10.1038/nature01829
506 Vočadlo, L., Dobson, D. P., & Wood, I. G. (2009). Ab initio calculations of the elasticity of hcp-Fe as a
507 function of temperature at inner-core pressure. *Earth and Planetary Science Letters*, *288*(3),
508 534–538. https://doi.org/10.1016/j.epsl.2009.10.015
509 Wang, S., & Tkalčić, H. (2020). Seismic event coda-correlation's formation: implications for global
510 seismology. *Geophysical Journal International*, *222*(2), 1283–1294.
511 https://doi.org/10.1093/gji/ggaa259
512 Waszek, L., & Deuss, A. (2011). Distinct layering in the hemispherical seismic velocity structure of
513 Earth's upper inner core. *Journal of Geophysical Research: Solid Earth*, *116*(B12).
514 https://doi.org/10.1029/2011JB008650

Wenk, H.-R., Matthies, S., Hemley, R. J., Mao, H.-K., & Shu, J. (2000). The plastic deformation of iron at pressures of the Earth's inner core. *Nature*, *405*(6790), 1044–1047. https://doi.org/10.1038/35016558

Woodhouse, J. H., Giardini, D., & Li, X.-D. (1986). Evidence for inner core anisotropy from free oscillations. *Geophysical Research Letters*, *13*(13), 1549–1552. https://doi.org/10.1029/GL013i013p01549

Wookey, J., & Helffrich, G. (2008). Inner-core shear-wave anisotropy and texture from an observation of PKJKP waves. *Nature*, *454*(7206), 873–876. https://doi.org/10.1038/nature07131

Yee, T.-G., Rhie, J., & Tkalčić, H. (2014). Regionally heterogeneous uppermost inner core observed with Hi-net array. *Journal of Geophysical Research: Solid Earth*, *119*(10), 7823–7845. https://doi.org/10.1002/2014JB011341

Yoshida, S., Sumita, I., & Kumazawa, M. (1996). Growth model of the inner core coupled with the outer core dynamics and the resulting elastic anisotropy. *Journal of Geophysical Research: Solid Earth*, *101*(B12), 28085–28103. https://doi.org/10.1029/96JB02700

Geophysical Research Letters

Supporting Information for

Shear-wave Anisotropy in the Earth's Inner Core

Sheng Wang[1], Hrvoje Tkalčić [1]

[1]Research School of Earth Sciences, The Australian National University, ACT 2601, Australia.

Contents of this file

Methods

Computation of earthquake coda-correlation wavefield

We compute earthquake coda-correlation wavefield following Phạm et al. (2018) and Wang and Tkalčić (2020). First, for global events and receivers (Figure S1), we select late-coda recordings in 3-9 h after events' origin time. We perform temporal normalization to suppress surface waves and spectral whitening to balance energy across the entire frequency band (Phạm et al., 2018). Then, we compute cross-correlation functions for recordings at each pair of receivers. We select the events close to the great-circle

555 plane passing through the two receivers due to their dominant and constructive contribution to coda-
556 correlation's formation (Wang & Tkalčić, 2020). We empirically discard the events being spherically
557 farther than 15° from the great-circle plane (Figures 2c,e,g). For two receivers at the same location, the
558 great-circle plane passes through the receivers and an event. Finally, we bin and stack the correlation
559 functions with respect to the inter-receiver distance and filter the stacked correlograms with a 15-50 s
560 (0.02-0.067 Hz), second-order, zero-phase bandpass filter.
561
562
563 *Grouping coda-correlation functions for different I2-J stacks*
564 We group correlation functions based on the geometry of events and receiver pairs. As shown in Figures
565 2 and S2, we can define a great-circle plane passing through the two receivers for each receiver pair. For
566 two receivers at the same location, the great-circle plane passes through the receivers and an event. For
567 each great-circle plane, we can define an angle φ for which $90° - \varphi$ is the angle between the plane's
568 normal and the Earth's rotation axis. We select receiver pairs having φ in the same bin (Figure S3), and
569 then we use those receiver pairs to compute I2-J stacks. For varied φ, we get different I2-J correlograms
570 (Figures 3 and S4), and they sample the IC differently (Figure 2).
571
572 Figure S5 shows the histograms for the number of receiver pairs relative to angle φ and inter-receiver
573 distance. There is a cliff-like change for φ crossing ~56°. That is because there is a limited number of
574 stations close to the equator. Most stations, especially the USArray stations, the stations in East Asia and
575 Europe, are at medium and high latitudes (Figure S1). The great-circle plane defined by any two
576 receivers cannot be close to the equator plane (φ=90°). Specifically, the southernmost stations of the
577 USArray are at latitudes ~30°N (Figure S1), and hence the largest φ for great-circle-planes defined by
578 any two USArray stations is ~60°. Given the dominance of USArray stations, there is a sharp reduction
579 near 56° in Figure S5. The column spike for $\varphi \sim 69°$ and inter-receiver distance ~15° corresponds to the
580 cross-correlations between two networks. The two networks are at ~20° N and are ~15° away from each
581 other. Several local-scale networks match such criteria, such as the Arabian Peninsula and East Africa
582 networks or Central America and the Caribbean Sea networks.
583
584

Slant-stack analysis

We perform slant stacking to transform the coda-correlation wavefield in distance-time (x-t) domain into slowness-delay time (τ-p) domain (Chapman, 1981):

$$s(\tau, p) = \sum_i c(\tau + p(x_i - x_0), x_i), \quad (1)$$

in which $c(t, x)$ represents coda-correlation correlograms, and $s(\tau, p)$ the slant stacks. To form a slant stack, each waveform $c(t,\ x_i)$ at a distance x_i is shifted in time by $p(x_i - x_0)$, and then all shifted waveforms are stacked together. The time shift depends on the reference distance x_0. For I2-J slant stacks, we choose $x_0 = 0°$. We search for the maximal amplitude point (τ_0, p_0) that corresponds to the optimal stack. The τ_0 and p_0 correspond to the time and slowness of I2-J at 0°, respectively. We choose x_0 =20° for PcP* slant stacks and the resultant τ_0 and p_0 correspond to the time and slowness of PcP* at 20°. Also, from two-dimensional slant stacks, we can extract the waveform stack $s(\tau, p_0)$ that are time series with the obtained p_0. The waveform stacks for I2-J and PcP* are shown in Figures 3, S6-S8.

The correlation feature I2-J has two branches in correlograms (Figure S4). We only use the lower branch of the I2-J cusp for slant-stacking analysis. That brings better accuracy and reliability for several reasons. As shown in Figure 3, the lower branch is visible in a larger distance range than the upper branch. Second, the lower branch is less contaminated by the strong feature PcP* than the upper branch. Third, the I2-J lower branch has a negative moveout while the PcP* presents a positive one, making them distinctive in the τ-p domain.

Bootstrap experiments

Due to the complex composition of J waves in forming I2-J stacks, we perform bootstrap experiments to test the stability of time measurements from the coda-correlation wavefield. We re-compute correlograms 200 times with random samples of receiver pairs, and then for each correlogram, we compute slant stacks and waveform stacks for I2-J and PcP*. As shown in Figure S8, the I2-J time variation between φ=40°-60° and φ=60°-80° is stable. Similarly, the PcP* time is stable, and it is nearly invariant between φ=40°-60° and φ=60°-80°.

Evaluation of IC shear-wave speed at different directions

We compute coda-correlation stacks for different φ ranges (Figure 2). We note that for φ angles varying from the equatorial to polar, I2-J corresponds to J waves sampling the IC in fundamentally different ways (Figures 2d,e,f). Namely, in a plane defined by φ, J waves propagating at different angles ξ in the interval from φ to 90° (Figures 2 and S2) contribute to the I2-J stack. The observed I2-J travel time corresponds to an averaged J wave speed at different ξ angles.

Specifically, for the bin φ=40°-60°, the I2-J is a result of J waves for ξ=40°-90°, and for the bin φ=60°-80°, the I2-J is a result of ξ=60°-90°. Accordingly, the ~5 s time difference between φ=40°-60° and φ=60°-80° (Figure 3) represents J-wave travel-time difference between ξ=40°-90° and ξ=60°-90°. For that, J waves must be faster for at least ~5 s at ξ=40°-60° (oblique angles relative to the Earth's rotation axis) than at ξ=60°-90° (equatorial angles).

Calculation of IC shear-wave speed

We calculate the shear wave speed for an anisotropic IC with low-order harmonics approximations following Song (1997):

$$\rho V_{S1}^2 = C_{44}(sin^4\xi + cos^4\xi) + (C_{11} + C_{33} - 2C_{44} - 2C_{13})sin^2\xi cos^2\xi, \quad (2)$$

$$\rho V_{S2}^2 = \frac{(C_{11}-C_{12})}{2} sin^2\xi + C_{44}cos^2\xi, \quad (3)$$

in which V_{S1} and V_{S2} are IC shear waves with polarization parallel to meridians and the equator, respectively, ρ the density, ξ the angle between J-wave ray paths and the Earth's rotation axis, and C_{11}, C_{33}, C_{44}, C_{12}, $C_{13}$the elastic constants for a cylindrically anisotropic (or transversely isotropic) medium:

$$\begin{bmatrix} C_{11} & C_{12} & C_{13} & C_{14} & C_{15} & C_{16} \\ & C_{22} & C_{23} & C_{24} & C_{25} & C_{26} \\ & & C_{33} & C_{34} & C_{35} & C_{36} \\ & & & C_{44} & C_{45} & C_{46} \\ & & & & C_{55} & C_{56} \\ & & & & & C_{66} \end{bmatrix} = \begin{bmatrix} c_{1111} & c_{1122} & c_{1133} & c_{1123} & c_{1113} & c_{1112} \\ & c_{2222} & c_{2233} & c_{2223} & c_{2213} & c_{2212} \\ & & c_{3333} & c_{3323} & c_{3313} & c_{3312} \\ & & & c_{2323} & c_{2313} & c_{2312} \\ & & & & c_{1313} & c_{1312} \\ & & & & & c_{1212} \end{bmatrix}, \quad (4)$$

in which (c_{ijkl}) $i,j,k,l = 1,2,3$ represents the tensor for elastic constants. We calculate the moduli for models with different crystal alignments using the coordinate transformation law (Auld, 1990):

$$c_{mnop} = a_{mi}a_{nj}a_{ok}a_{pl}c_{ijkl} \ \ (i,j,k,l,m,n,o,p = 1,2,3), \quad (5)$$

in which (a_{ij}) is the matrix for coordinate transformation. The elastic constants for different IC iron models are in Supplementary Table 1. We calculate the averaged shear wave speed following Lin et al., (2010) and Mao et al., (2008):

$$\frac{2}{V_S^3} = \frac{1}{V_{S1}^3} + \frac{1}{V_{S2}^3}, \quad (6)$$

in which V_{S1} and V_{S2} are speed of J waves of the two polarizations. Calculation results for different models are in Figure S9.

Synthetic experiments for IC shear wave stacks at different φ angles

We perform synthetic experiments to show how IC shear-wave anisotropy can decrease the amplitude of I2-J stacks when φ approaches 0°. We set an IC model made of a single crystal of hcp structure (Figure 4 and Table S1). We then calculate the relative travel times and produce synthetic waveforms for J waves propagating in different directions. We do not consider the compressional-wave anisotropy in the IC, because the compressional waves (I waves) contributing to the I2-J feature sample the topmost IC at maximal depths less than 10 km below the ICB (Figure S11c). Apart from that, the thin layer (thickness of a few tens of kilometers) in the upper IC was suggested to be quasi-isotropic or weakly anisotropic (less than 1%) (e.g., Shearer, 1994; Song & Helmberger, 1995). In the calculation, we take ellipticity into account. We use Ricker wavelets to represent synthetic waveforms by shifting them with respect to the calculated travel times. They are bandpass filtered in the interval 15-50 s, which is the dominant frequency range for coda-correlation wavefield. Then, for each angle φ, we calculate the composition of J waves for varied angle ξ (Figures S10a-b). The composition is described by the probability density function (PDF) with respect to angle ξ (the angle between J wave ray paths and the rotation axis). Finally, we calculate waveform stacks (Figures S10d,f,h) based on the synthetics and the PDFs. The stacking is weighted by the PDFs. We perform the tests for J waves with polarization parallel to meridians (Figures S10c-d) and the equator (Figures S10E-F), and the averaged J waves (Figures S10g-h).

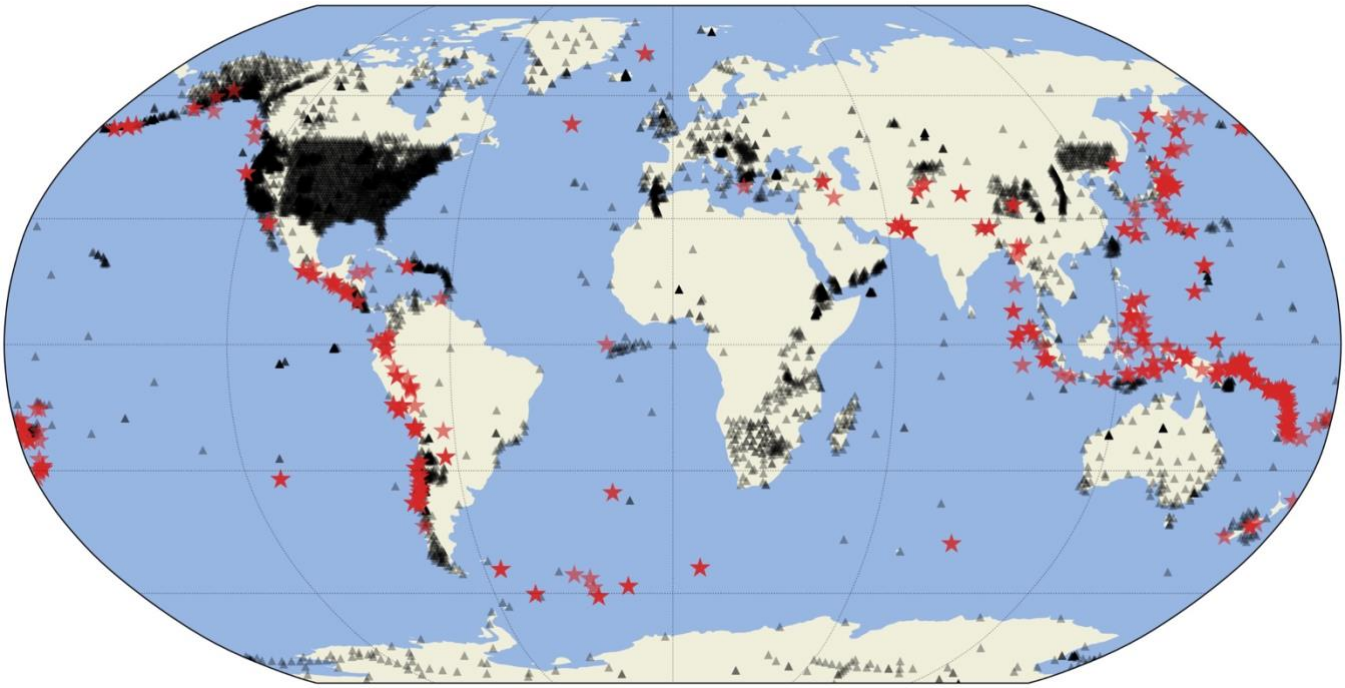

Figure S1. Global distributions of events (red stars) and stations (black triangles) used in this study. Mw≥6.8 earthquakes in 2010–2019 from the National Earthquake Information Center (NEIC) catalog (https://pubs.er.usgs.gov/publication/70016044) are used, as listed in Table S2. Seismic waveform data are retrieved from IRIS DMC (https://ds.iris.edu/ds/nodes/dmc/data). Stations are from networks identified according to FDSN (https://www.fdsn.org/networks/): 1P, 2H, 2K, 3J, 4F, 5A, 6A, 6D, 6E, 7A, 7C, 8A, 9C, 9D, AC, AD, AE, AF, AI, AK, AT, AU, AV, AZ, BC, BE, BK, BL, BN, BX, C, C1, CA, CB, CC, CH, CI, CK, CM, CN, CU, CZ, DK, DR, EI, EP, ER, ES, EV, G, GB, GE, GG, GR, GS, GT, HK, HL, HT, HV, HW, IC, II, IM, IO, IP, IU, IW, JP, KC, KG, KN, KO, KP, KR, KS, KW, KZ, LB, LD, LI, LM, LX, MB, MC, MG, MI, MM, MN, MS, MU, MX, MY, N4, NA, NE, NJ, NK, NL, NM, NN, NO, NR, NU, OE, OH, OK, ON, OO, OV, PB, PE, PI, PL, PM, PN, PO, PP, PR, PS, PT, PY, RB, RM, RO, RV, S1, SB, SC, SL, SS, SV, TA, TC, TM, TR, TS, TT, TW, TX, UK, UO, US, UU, UW, VE, WC, WI, WM, WY, X1, X3, X5, X9, XB, XD, XE, XF, XH, XI, XN, XP, XR, XS, XU, XV, XW, XZ, Y2, Y5, Y6, YB, YD, YE, YF, YG, YH, YL, YM, YN, YP, YS, YT, YW, YY, YZ, Z1, Z2, Z4, Z5, Z6, ZC, ZM, ZN, ZP, ZT, ZV.

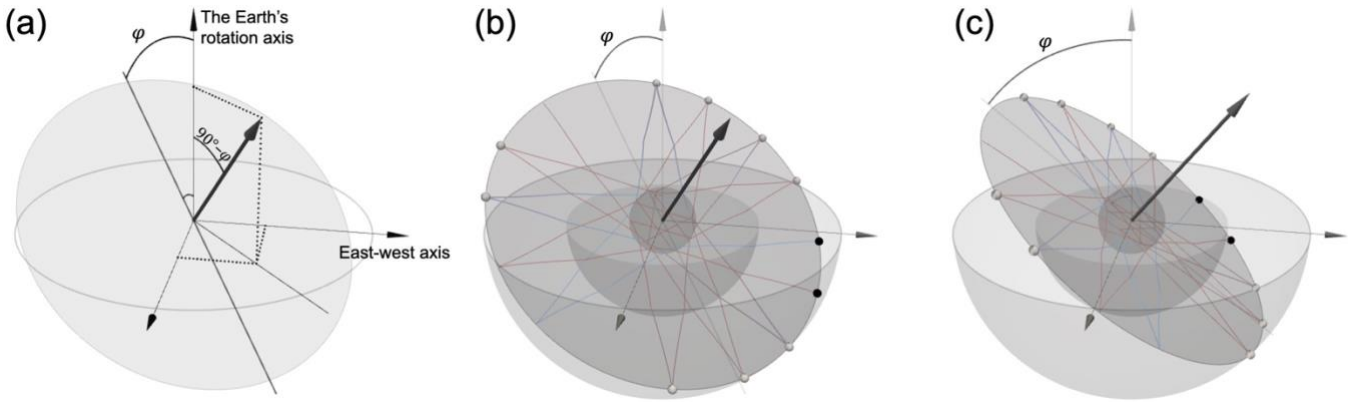

Figure S2. (**a**) A great-circle plane is described by its normal vector (black arrow) in three dimensions. φ is the angle between the great-circle plane and the Earth's rotation axis. $90°-\varphi$ is the angle between the normal vector and the rotation axis. (**b**) A great-circle plane passing through two receivers (black spheres) and events (white spheres). (**c**) Another great-circle plane with the same angle φ as in (b) but with a different normal vector. The receiver pairs are binned in ranges with respect to φ (Figure S3) to form nine I2-J stacks (Figure S4).

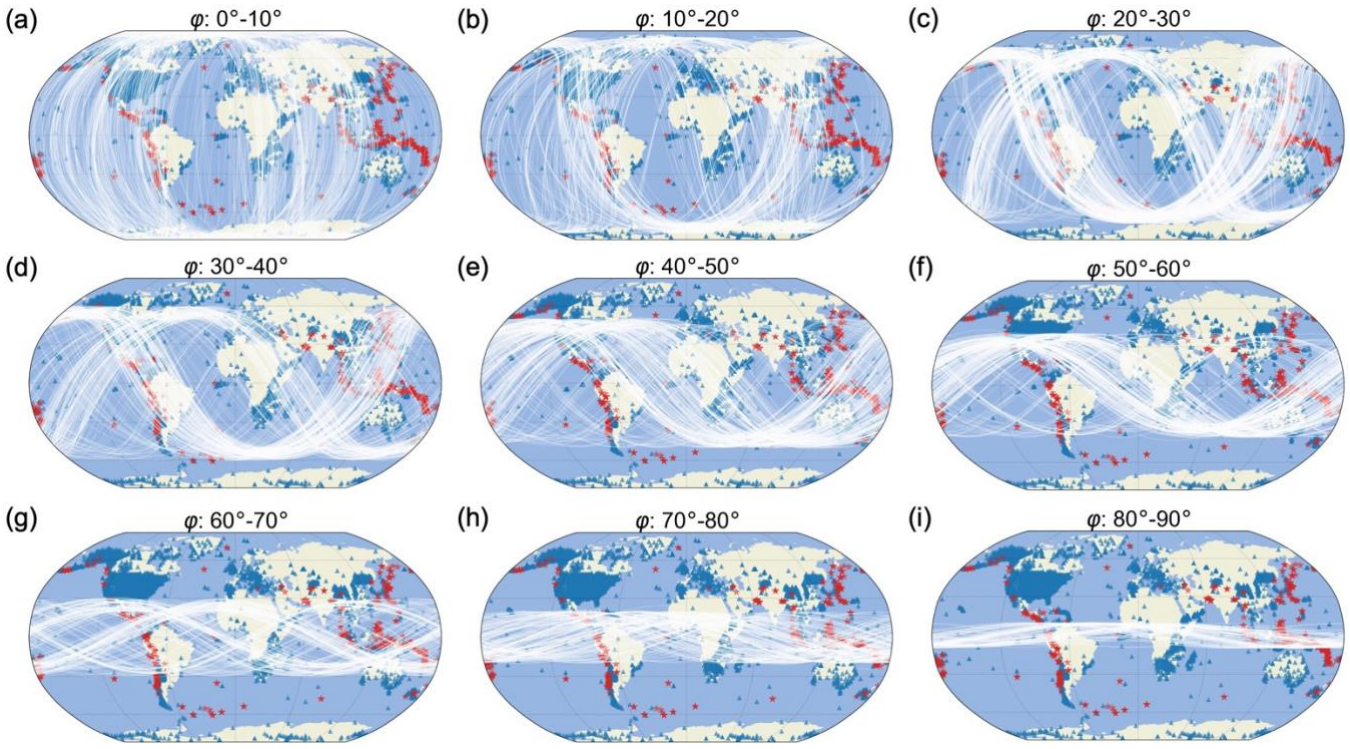

Figure S3. Great-circle planes (white lines) for different angle φ ranges: (a) 0°-10°, (b) 10°-20°, (c) 20°-30°, (d) 30°-40°, (e) 40°-50°, (f) 50°-60°, (g) 60°-70°, (h) 70°-80°, (i) 80°-90°. The angle φ is defined in Figure 2 and Figure S2. See Methods for grouping of correlograms for the angle φ. We plot randomly downsampled great-circle planes instead of all planes to avoid intense overlapping.

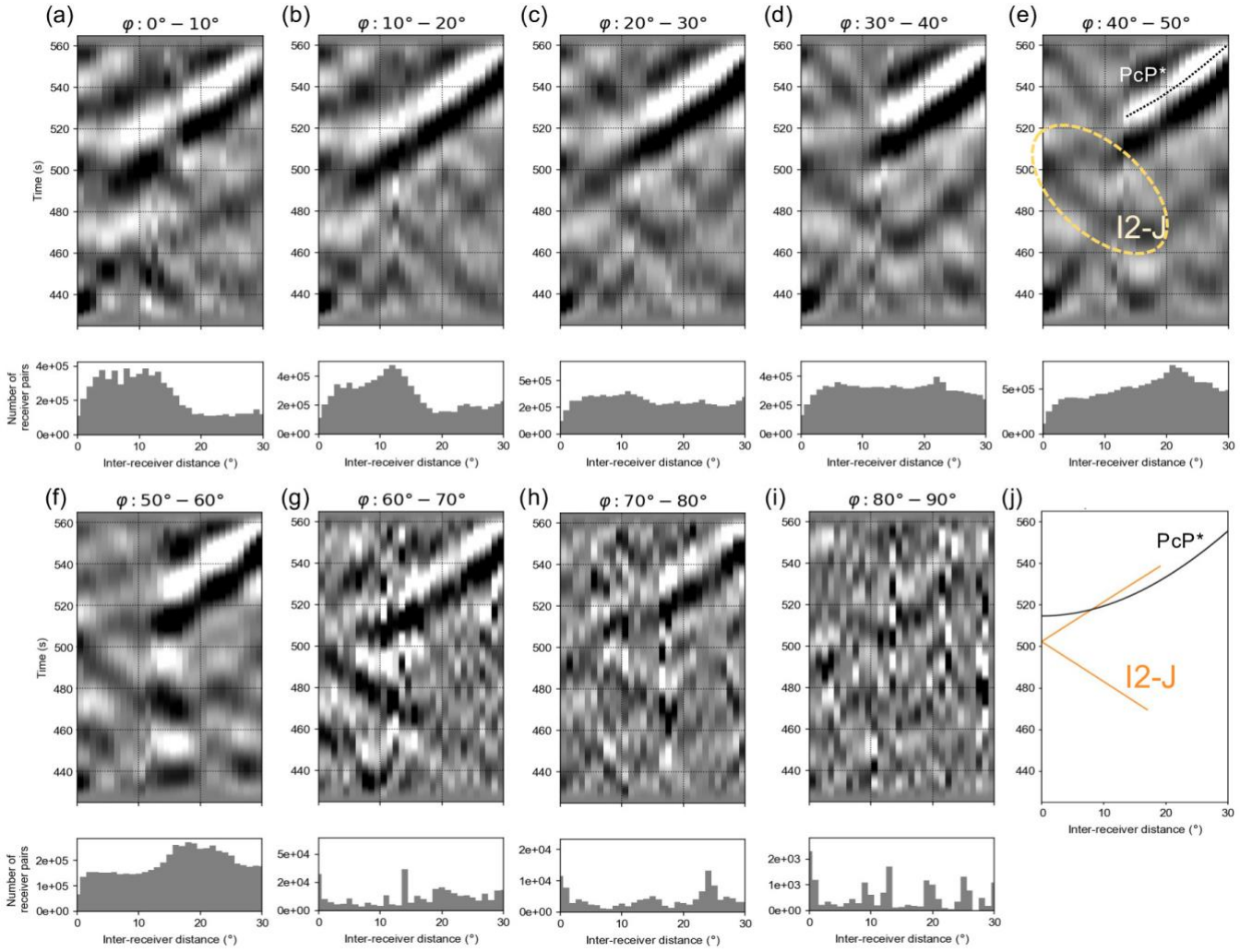

Figure S4. Earthquake Coda correlograms and histograms of receiver pair numbers for nine angle φ ranges: (**a**) 0°-10°, (**b**) 10°-20°, (**c**) 20°-30°, (**d**) 30°-40°, (**e**) 40°-50°, (**f**) 50°-60°, (**g**) 60°-70°, (**h**) 70°-80°, (**i**) 80°-90°. φ is the angle between a great-circle plane and the Earth's rotation axis, as defined in Figures 2 and S2. The orange ellipse (shown only in (e) to avoid overlapping with the correlogram features for the sake of clarity) indicates the I2-J cusp sensitive to the IC shear-wave speed. The feature PcP*, sensitive to mantle structure, CMB topography, and Earth's ellipticity, is indicated by the black dotted line. Positive amplitudes are in white, and negative amplitudes are in black shades. The intensity of the black or white indicates the amplitude strength. (**j**) Theoretical I2-J and PcP* time curves based on Tkalčić & Phạm (2018).

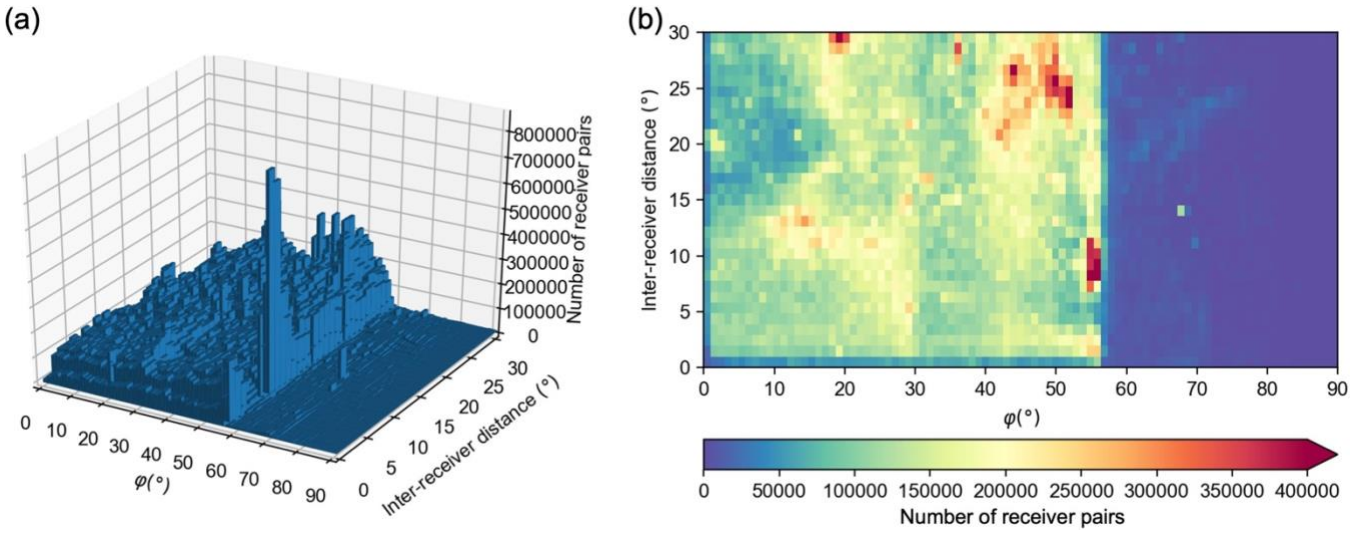

Figure S5. (**a**) 3D histogram of the number of receiver pairs relative to angle φ (as defined in Figs. 2 and S2) and inter-receiver distance. See the Methods section for the cliff-like change for φ~60° and the column spike for φ~69° and inter-receiver distance ~15°. (**b**) Isogram of the 3D histogram in (a).

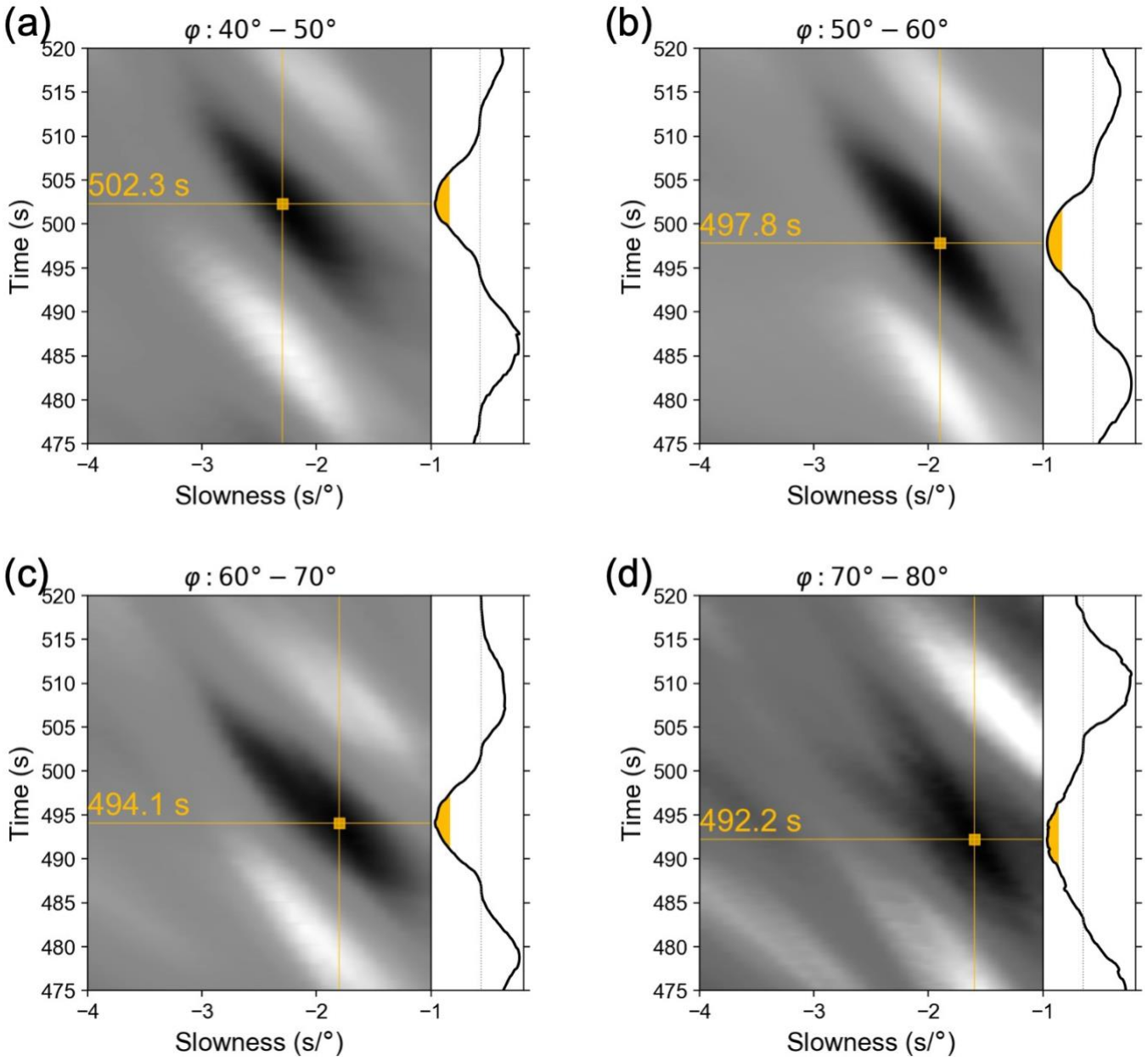

Figure S6. I2-J slant-stacks for four angle φ ranges: (a) 40°-50°, (b) 50°-60°, (c) 60°-70°, (d) 70°-80°. The yellow dots correspond to the lower branch of the I2-J cusp. φ is the angle between a great-circle plane and the Earth's rotation axis, as defined in Figures 2 and S2. Each slant stack is normalized with respect to the maximal amplitude. Details of the slant-stack method are in Methods section.

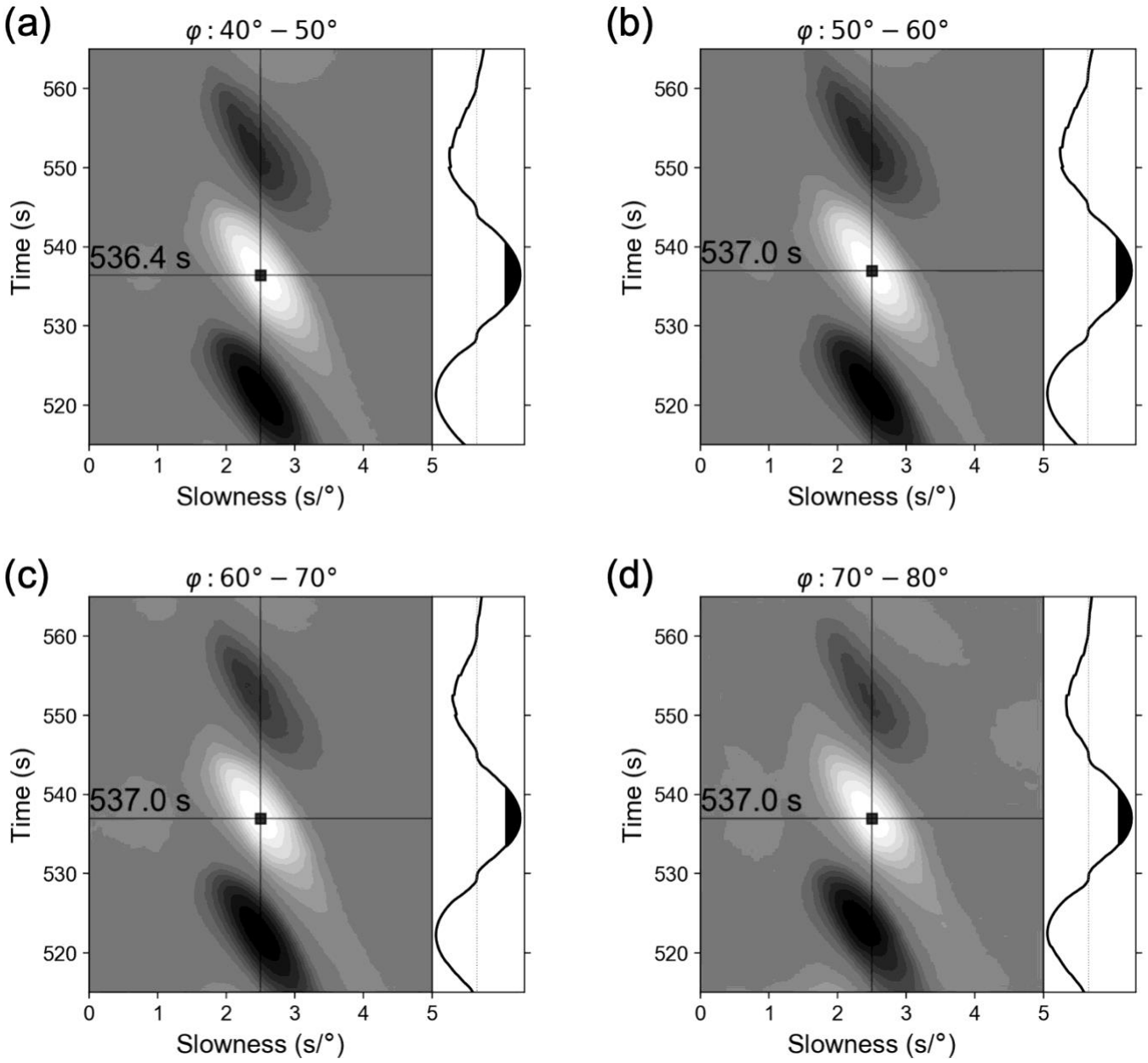

Figure S7. PcP* slant-stacks for four angle φ ranges: (a) 40°-50°, (b) 50°-60°, (c) 60°-70°, (d) 70°-80°. The φ is the angle between a great-circle plane and the Earth's rotation axis, as defined in Figures 2 and S2. Each slant stack is normalized with respect to the maximal amplitude. Details of the slant-stack method are in Methods section.

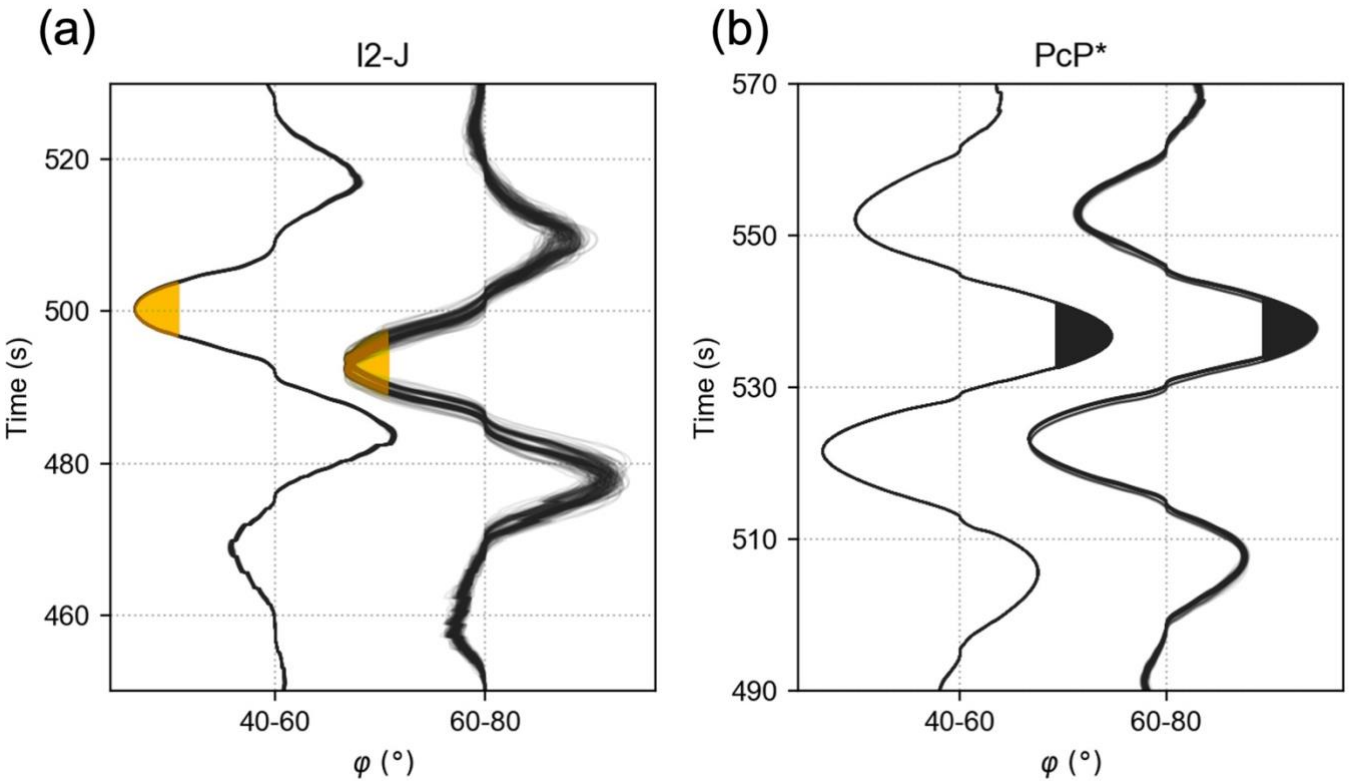

Figure S8. Bootstrap experiments for travel time measurements of I2-J (a) and PcP* (b). See Methods section for details of bootstrap experiments. Waveform stacks for (a) I2-J and (b) PcP* correlogram features are extracted from the slant-stacks. Each waveform stack (represented by black lines) corresponds to a single random resampling. Colored areas correspond to stack amplitudes greater than 80% of the maximum.

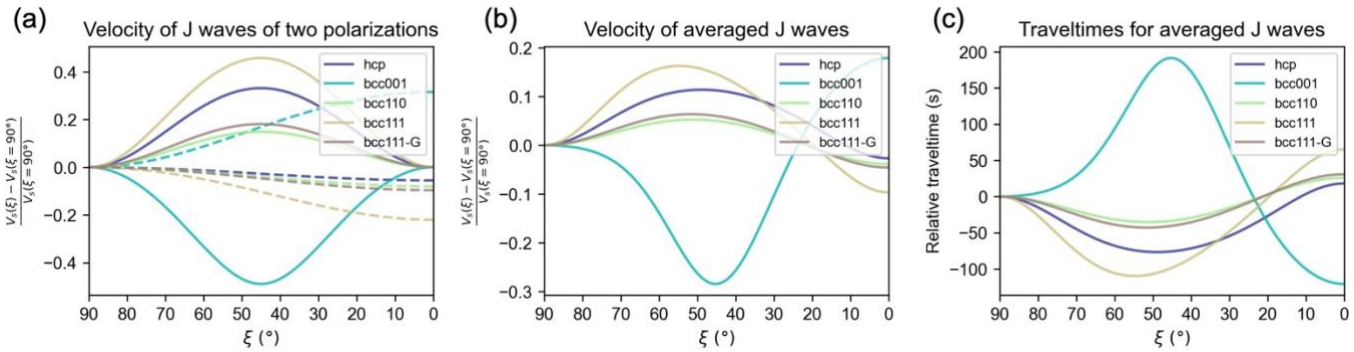

Figure S9. (**a**) Fractional J-wave speed (with respect to the speed in the equatorial plane) for two polarizations as a function of the angle ξ defined in Figure 4 for a cylindrically anisotropic inner core. The solid lines represent the J waves with the polarization parallel to meridians, and the dash lines represent the J waves with the polarization parallel to the equator. The colors represent different iron crystal models, as listed in Table S1. The 3D iron crystal models of hcp and bcc are illustrated in Figure 4. (**b**) Same as (a) but for averaged (both polarizations) J waves. (**c**) Relative travel time for averaged J waves traveling along the IC diameters. See Methods section for calculations of J-wave speed given elastic properties of an iron crystal model.

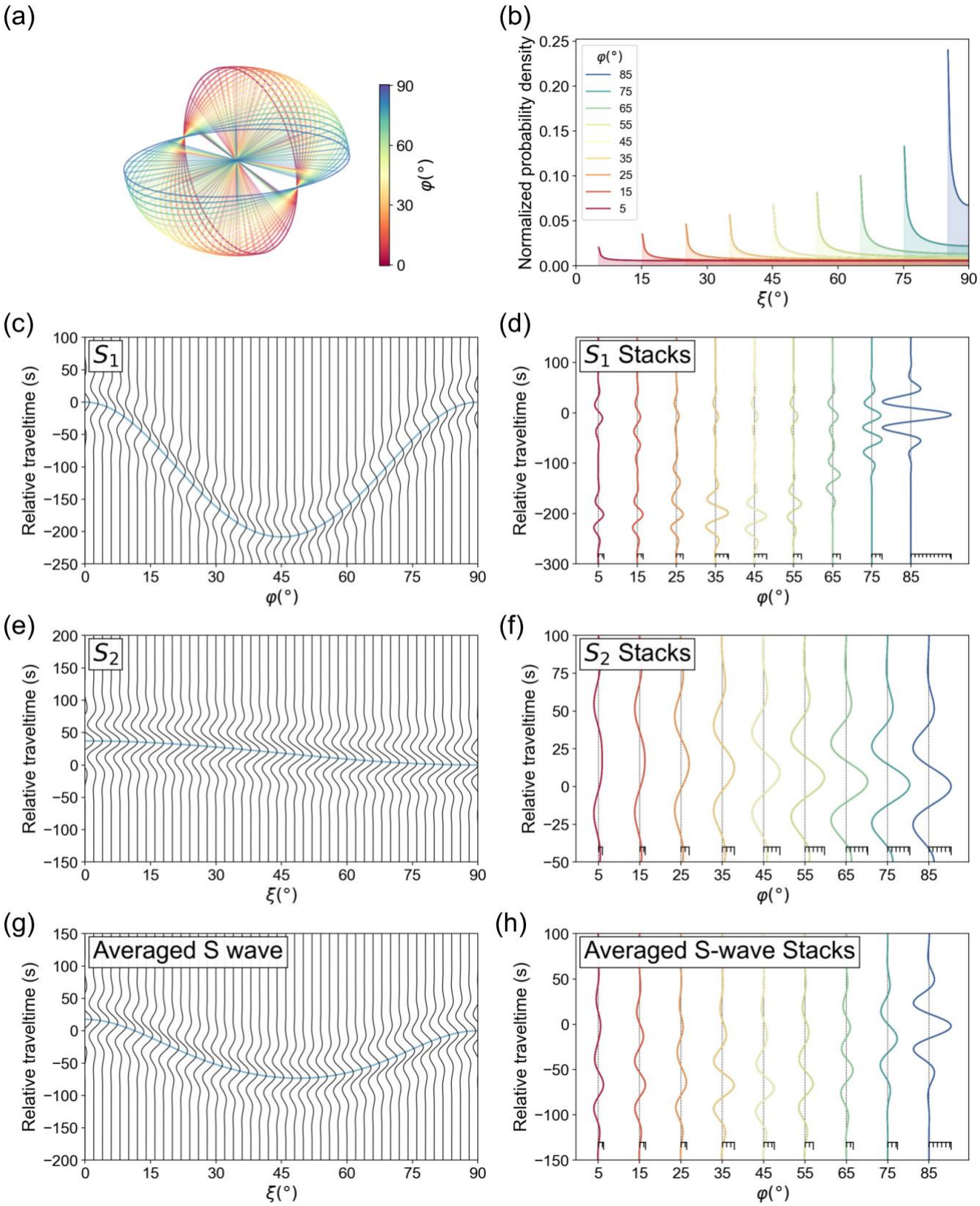
(a)
90
60
30
0
φ(°)
(b)
Normalized probability density
φ(°)
85
75
65
55
45
35
25
15
5
ξ(°)
(c)
S1
Relative traveltime (s)
φ(°)
(d)
S1 Stacks
Relative traveltime (s)
φ(°)
(e)
S2
Relative traveltime (s)
ξ(°)
(f)
S2 Stacks
Relative traveltime (s)
φ(°)
(g)
Averaged S wave
Relative traveltime (s)
ξ(°)
(h)
Averaged S-wave Stacks
Relative traveltime (s)
φ(°)

Figure S10. Synthetic tests for I2-J stacks at different angles φ given an anisotropic inner core. (**a**) Inner-core shear-wave ray paths inside great-circle planes for varied angles φ shown in different colors. The φ is the angle between a great-circle plane and the Earth's rotation axis, as defined in Figures 2 and S2. (**b**) The probability density of inner-core shear-wave angle ξ for great-circle planes at different φ. The ξ is the angle between inner-core shear wave ray paths and the rotation axis. The shaded areas indicate the integrals of the probability density functions that correspond to the weighting-factors for computing the synthetic waveform stacks for different φ. (**c**) Synthetic waveforms of inner-core shear wave S_1 that propagate at different angles ξ. The S_1 has the polarization parallel the meridians and passes through the Earth's center. The relative travel time curve (blue line) is based on the hcp iron model in Figure 4 and Table S1 and corrected for the Earth's ellipticity. Other iron crystal models have similar behavior. We use Ricker wavelets bandpass-filtered in the 15-50 s range, which is the dominant frequency range of the coda-correlation wavefield. (**d**) Stacked S_1 waveforms for different angles φ based on the probability density of ξ (b). The scale bars indicate the relative amplitude difference for waveform stacks for different angles φ. (**e**) Similar to (c) but for inner-core shear waves S_2 that have the polarization parallel to the equator. (**f**) Similar to (d) but for S_2 wave stacks. (**g**) Similar to (c) but for averaged shear waves in the inner core. The average uses the expression ${}^{2}/_{V_S} = {}^{1}/_{V_{S1}} + {}^{1}/_{V_{S2}}$(Lin et al., 2010; Mao et al., 2008) . (**h**) Similar to (d) but for averaged S-wave stacks.

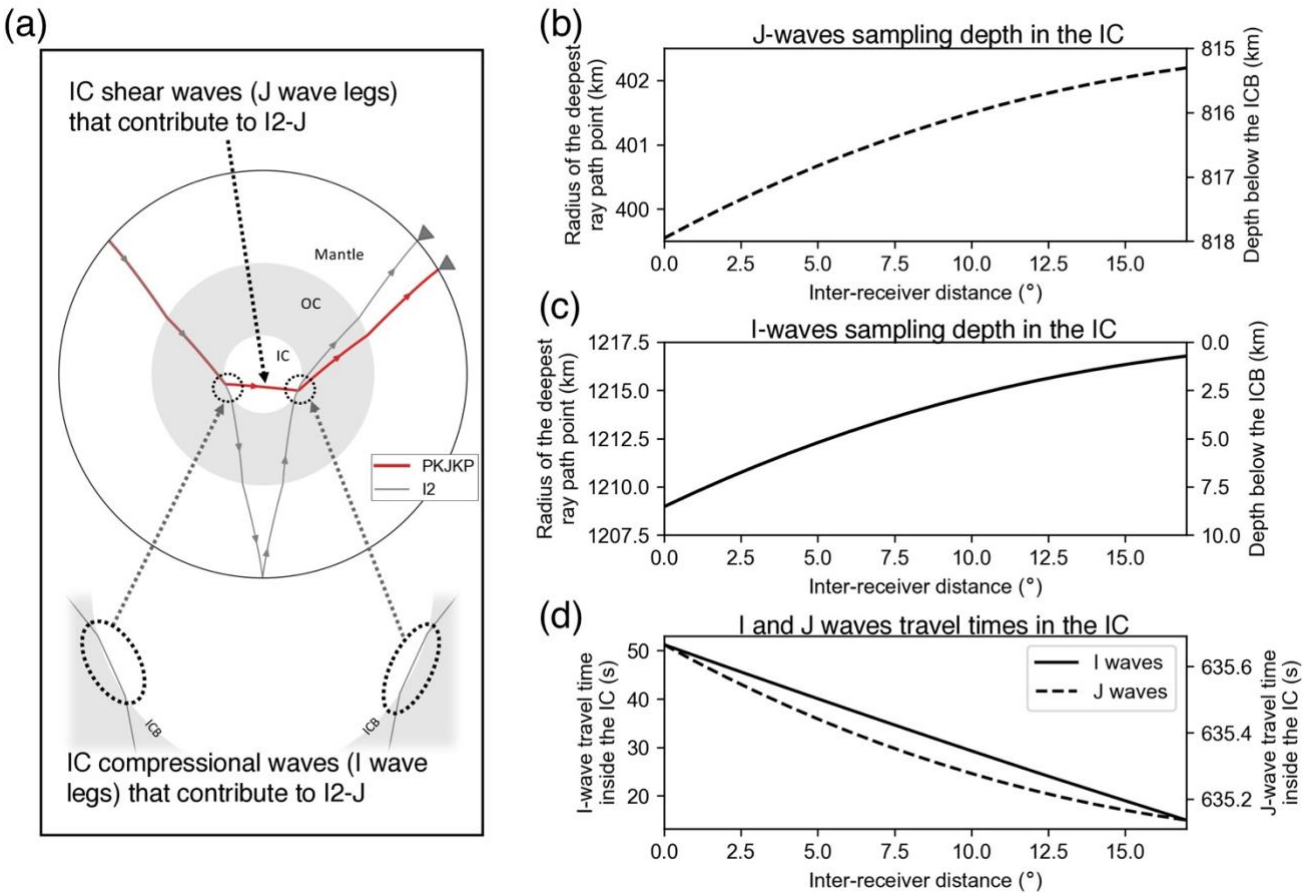

Figure S11. A sampling of the IC for shear waves and compressional waves that contribute to the coda-correlation feature I2-J. (**a**) Diagram for I2-J ray path. The I2-J is formed by the cross-correlation between PKIKPPKIKP (grey line) and PKJKP (red line). The IC shear waves (J waves) that contribute to I2-J are indicated with a dashed arrow. The insets show the IC compressional waves (I waves) that contribute to I2-J. (**b**) Radius/depth of the deepest ray path point for J waves contributing to I2-J as a function of inter-receiver distance. We use the reference model ak135 (Kennett et al., 1995) for computing the ray path. We choose the lower branch of the I2-J to analyze the time variations (see Methods section in the supporting information). (**c**) The same as (b) but for I waves contributing to I2-J. (**d**) The total travel time for J and I (double legs) waves that contribute to the I2-J.

782
783
784 **Table S1.** Elastic properties of inner-core iron crystal models used in this study. The elastic properties
785 for hcp and bcc001 are provided by Mattesini et al. (2010), Romanowicz et al. (2016), and Vočadlo et al.
786 (2009). We compute the elastic properties for bcc110 and bcc111 via rotating the bcc001 model
787 (Methods). bcc111-G corresponds to an imperfect alignment of the bcc111 crystal (see main text). The
788 anisotropy of S waves is $An(\%) = 200(S_{max} - S_{min})/(S_{max} + S_{min})$.

Iron model	ρ (g/cm3)	c11 (GPa)	c33	c44	c12	c13	Anisotropy of S (%)
hcp	13.543	1700	1769	200	1252	1025	13.5
bcc001	13.559	1715	1561	365	1293	1448	48.9
bcc110	13.559	1831	1870	211	1332	1293	9.0
bcc111	13.559	1870	1973	159	1345	1242	25.1
bcc111-G	13.559	1836	1882	205	1334	1287	10.8

789
790
791 **Table S2.** List of events used in this study.
792

Table S2. List of events used in this study				
Longitude(°)	Latitude(°)	Depth (km)	Magnitude(Mw)	Origin Time
125.17	6.7	18	6.8	2019-12-15T06:11:51
126.42	1.62	33	7.1	2019-11-14T16:17:40
104.79	-7.28	49	6.9	2019-08-02T12:03:27
-72.31	-34.24	25	6.8	2019-08-01T18:28:07
128.03	-0.59	19	7.2	2019-07-14T09:10:51
126.19	0.51	35	6.9	2019-07-07T15:08:40
129.17	-6.41	212	7.3	2019-06-24T02:53:39
-178.1	-30.64	46	7.3	2019-06-15T22:55:04
-75.27	-5.81	123	8	2019-05-26T07:41:15
152.6	-4.05	10	7.6	2019-05-14T12:58:25
146.45	-6.97	146	7.1	2019-05-06T21:19:37
122.58	-1.81	15	6.8	2019-04-12T11:40:49
-70.16	-14.71	267	7	2019-03-01T08:50:42
-77.05	-2.19	145	7.5	2019-02-22T10:17:23
-71.59	-8.14	570	6.8	2019-01-05T19:25:38
126.92	5.9	60	7	2018-12-29T03:39:09
164.7	55.1	17	7.3	2018-12-20T17:01:55
-26.39	-58.55	133	7.1	2018-12-11T02:26:29

169.43	-21.95	10	7.5	2018-12-05T04:18:08
-149.96	61.35	47	7.1	2018-11-30T17:29:29
-178.93	-17.87	540	6.8	2018-11-18T20:25:46
20.56	37.52	14	6.8	2018-10-25T22:54:52
-129.29	49.34	10	6.8	2018-10-22T06:16:26
151.21	-5.7	39	7	2018-10-10T20:48:20
119.85	-0.26	20	7.5	2018-09-28T10:02:45
-179.37	-31.75	115	6.9	2018-09-10T04:19:02
179.35	-18.47	671	7.9	2018-09-06T15:49:18
170.13	-22.03	21	7.1	2018-08-29T03:51:56
-70.83	-11.04	630	7.1	2018-08-24T09:04:08
-62.9	10.77	147	7.3	2018-08-21T21:31:47
116.63	-8.32	21	6.9	2018-08-19T14:56:27
-178.15	-18.11	600	8.2	2018-08-19T00:19:40
116.44	-8.26	34	6.9	2018-08-05T11:46:38
-63.01	-20.66	559	6.8	2018-04-02T13:40:34
151.5	-5.53	35	6.9	2018-03-29T21:25:36
153.2	-4.38	23	6.8	2018-03-08T17:39:51
142.75	-6.07	25	7.5	2018-02-25T17:44:44
-97.98	16.39	22	7.2	2018-02-16T23:39:39
-149.17	56	14	7.9	2018-01-23T09:31:40
-74.71	-15.77	39	7.1	2018-01-14T09:18:45
-83.52	17.48	19	7.5	2018-01-10T02:51:33
168.67	-21.32	10	7	2017-11-19T22:43:29
45.96	34.91	19	7.3	2017-11-12T18:18:17
-173.17	-15.32	10	6.8	2017-11-04T09:00:19
-98.49	18.55	48	7.1	2017-09-19T18:14:38
-93.9	15.02	47	8.2	2017-09-08T04:49:19
168.86	54.44	10	7.7	2017-07-17T23:34:13
-90.97	13.72	38	6.8	2017-06-22T12:31:03
-92.01	14.91	93	6.9	2017-06-14T07:29:04
167.38	-14.59	169	6.8	2017-05-09T13:52:10
125.07	5.5	26	6.9	2017-04-28T20:23:17
-72.06	-33.04	28	6.9	2017-04-24T21:38:30
-178.8	-23.26	414	6.9	2017-02-24T17:28:44
155.17	-6.25	135	7.9	2017-01-22T04:30:22
122.62	4.48	627	7.3	2017-01-10T06:13:48
176.05	-19.37	12	6.9	2017-01-03T21:52:30

-73.94	-43.41	38	7.6	2016-12-25T14:22:27
153.52	-4.5	95	7.9	2016-12-17T10:51:10
161.13	-10.75	20	6.9	2016-12-09T19:10:06
161.33	-10.68	40	7.8	2016-12-08T17:38:46
-88.9	11.91	10	6.9	2016-11-24T18:43:47
173.05	-42.74	15	7.8	2016-11-13T11:02:56
148.89	-6	42	6.8	2016-10-17T06:14:58
-178.24	-19.78	596	6.9	2016-09-24T21:28:41
179.15	-37.36	19	7	2016-09-01T16:37:57
152.79	-3.69	476	6.8	2016-08-31T03:11:34
-17.83	-0.05	10	7.1	2016-08-29T04:29:57
94.57	20.92	82	6.8	2016-08-24T10:34:54
-31.88	-55.28	10	7.4	2016-08-19T07:32:22
173.12	-22.48	16	7.2	2016-08-12T01:26:36
145.51	18.54	196	7.7	2016-07-29T21:18:24
-26.93	-56.24	78	7.2	2016-05-28T09:46:59
-178.2	-21.97	406	6.9	2016-05-28T05:38:50
-79.62	0.49	30	6.9	2016-05-18T16:46:43
167.38	-16.04	24	7	2016-04-28T19:33:24
-79.92	0.38	21	7.8	2016-04-16T23:58:36
130.75	32.79	10	7	2016-04-15T16:25:06
94.86	23.09	136	6.9	2016-04-13T13:55:17
166.85	-14.32	26	6.9	2016-04-03T08:23:52
94.33	-4.95	24	7.8	2016-03-02T12:49:48
158.55	53.98	177	7.2	2016-01-30T03:25:12
-153.34	59.62	126	7.1	2016-01-24T10:30:29
129.51	-4.11	21	6.9	2015-12-09T10:21:48
72.78	38.21	22	7.2	2015-12-07T07:50:05
85.09	-47.62	35	7.1	2015-12-04T22:25:00
-71.02	-10.06	621	7.6	2015-11-24T22:50:54
-70.94	-10.54	606	7.6	2015-11-24T22:45:38
158.42	-8.9	13	6.8	2015-11-18T18:31:04
-72.06	-29.51	10	6.9	2015-11-11T02:46:19
-72.01	-29.51	12	6.9	2015-11-11T01:54:38
-71.45	-30.88	46	6.8	2015-11-07T07:31:43
70.37	36.52	231	7.5	2015-10-26T09:09:42
167.3	-14.86	135	7.1	2015-10-20T21:52:02
-71.43	-31.56	28	7	2015-09-16T23:18:41

-71.67	-31.57	22	8.3	2015-09-16T22:54:32
138.53	-2.63	48	7	2015-07-27T21:41:21
-169.45	52.38	29	6.9	2015-07-27T04:49:46
165.14	-10.4	11	7	2015-07-18T02:27:33
-17.16	-35.36	10	7	2015-06-17T12:51:32
140.49	27.84	664	7.8	2015-05-30T11:23:02
-156.43	56.59	73	6.8	2015-05-29T07:00:09
163.22	-11.11	10	6.8	2015-05-22T23:59:33
163.7	-11.06	11	6.9	2015-05-22T21:45:19
164.17	-10.88	11	6.8	2015-05-20T22:48:53
142.03	38.91	35	6.8	2015-05-12T21:12:58
86.07	27.81	15	7.3	2015-05-12T07:05:19
154.56	-7.22	10	7.1	2015-05-07T07:10:19
151.88	-5.46	55	7.5	2015-05-05T01:44:06
151.78	-5.2	44	6.8	2015-05-01T08:06:03
152.56	-4.73	41	7.5	2015-03-29T23:48:31
122.53	-7.3	552	7	2015-02-27T13:45:05
-31.9	52.65	17	7.1	2015-02-13T18:59:12
168.52	-17.03	220	6.8	2015-01-23T03:47:27
126.58	1.96	39	6.8	2014-11-26T14:33:43
126.52	1.89	45	7.1	2014-11-15T02:31:41
-177.76	-19.69	434	7.1	2014-11-01T18:57:22
-88.12	12.53	40	7.3	2014-10-14T03:51:34
-110.81	-32.11	17	7	2014-10-09T02:14:31
-73.57	-14.6	101	6.8	2014-08-24T23:21:45
146.17	0.83	13	6.9	2014-08-03T00:22:03
-178.4	-19.8	615	6.9	2014-07-21T14:54:41
-92.46	14.72	53	6.9	2014-07-07T11:23:54
178.74	51.85	109	7.9	2014-06-23T20:53:09
-177.72	-29.98	20	6.9	2014-06-23T19:19:15
155.02	-6.75	43	7.5	2014-04-19T13:28:00
-100.97	17.4	24	7.2	2014-04-18T14:27:24
8.72	-53.5	11	6.8	2014-04-15T03:57:01
162.05	-11.46	39	7.4	2014-04-13T12:36:19
162.15	-11.27	23	7.6	2014-04-12T20:14:39
155.05	-6.59	61	7.1	2014-04-11T07:07:23
-70.49	-20.57	22	7.7	2014-04-03T02:43:13
-70.94	-19.89	28	6.9	2014-04-01T23:57:58

-70.77	-19.61	25	8.2	2014-04-01T23:46:47
-125.13	40.83	16	6.8	2014-03-10T05:18:13
82.59	35.91	10	6.9	2014-02-12T09:19:49
-55	-53.95	12	7	2013-11-25T06:27:33
-46.4	-60.27	10	7.7	2013-11-17T09:04:55
144.66	37.16	35	7.1	2013-10-25T17:10:19
154.93	-6.45	35	6.8	2013-10-16T10:30:58
124.12	9.88	19	7.1	2013-10-15T00:12:32
65.5	27.18	12	6.8	2013-09-28T07:34:06
-74.51	-15.84	40	7.1	2013-09-25T16:42:43
65.5	26.95	15	7.7	2013-09-24T11:29:47
-175.23	51.54	29	7	2013-08-30T16:25:02
-25.07	-60.86	11	7.3	2013-07-15T14:03:39
153.93	-3.92	386	7.3	2013-07-07T18:35:30
153.22	54.89	598	8.3	2013-05-24T05:44:48
-177.23	-23.01	174	7.4	2013-05-23T17:19:04
145.29	18.73	602	6.8	2013-05-14T00:32:25
150.79	46.22	110	7.2	2013-04-19T03:05:52
62	28.03	80	7.7	2013-04-16T10:44:20
138.48	-3.52	66	7	2013-04-06T04:42:35
157.28	50.95	41	6.9	2013-02-28T14:05:50
-77.39	1.14	145	6.9	2013-02-09T14:16:07
166.02	-10.93	21	7.1	2013-02-08T15:26:38
165.97	-10.84	12	6.8	2013-02-08T11:12:11
164.88	-11.18	10	7.1	2013-02-06T01:23:19
165.11	-10.8	24	8	2013-02-06T01:12:25
143.09	42.77	107	6.9	2013-02-02T14:17:35
-70.65	-28.09	45	6.8	2013-01-30T20:15:43
129.82	-6.53	155	7.1	2012-12-10T16:53:08
143.95	37.89	31	7.3	2012-12-07T08:18:23
95.89	23	14	6.8	2012-11-11T01:12:38
-91.89	13.99	24	7.4	2012-11-07T16:35:46
-132.1	52.79	14	7.8	2012-10-28T03:04:08
-76.36	1.93	170	7.3	2012-09-30T16:31:35
-85.31	10.09	35	7.6	2012-09-05T14:42:07
126.64	10.81	28	7.6	2012-08-31T12:47:33
-10.61	71.44	14	6.8	2012-08-30T13:43:25
-88.59	12.14	28	7.3	2012-08-27T04:37:19

145.06	49.8	583	7.7	2012-08-14T02:59:38
147.12	-5.46	198	6.8	2012-04-17T07:13:49
-113.1	28.7	13	7	2012-04-12T07:15:48
92.46	0.8	25	8.2	2012-04-11T10:43:10
93.06	2.33	20	8.6	2012-04-11T08:38:36
-72.22	-35.2	41	7.1	2012-03-25T22:37:06
-98.23	16.49	20	7.4	2012-03-20T18:02:47
144.94	40.89	12	6.9	2012-03-14T09:08:35
167.13	-17.83	23	7.1	2012-02-02T13:34:40
93.21	2.43	19	7.2	2012-01-10T18:36:59
138.07	31.46	365	6.8	2012-01-01T05:27:55
146.81	-7.55	135	7.1	2011-12-14T05:04:58
125.62	27.32	225	6.9	2011-11-08T02:59:08
-75.97	-14.44	24	6.9	2011-10-28T18:54:34
43.51	38.72	18	7.1	2011-10-23T10:41:23
-176.24	-28.99	33	7.4	2011-10-21T17:57:16
88.16	27.73	50	6.9	2011-09-18T12:40:51
-179.53	-21.61	645	7.3	2011-09-15T19:31:04
169.72	-20.67	185	7	2011-09-03T22:55:40
-171.71	52.17	32	6.9	2011-09-02T10:55:53
126.75	-6.36	470	6.9	2011-08-30T06:57:41
-74.53	-7.64	147	7	2011-08-24T17:46:11
168.22	-18.31	28	7.1	2011-08-20T18:19:23
168.14	-18.36	32	7.2	2011-08-20T16:55:02
143.26	38.03	23	7	2011-07-10T00:57:10
-176.34	-29.54	17	7.6	2011-07-06T19:03:18
-171.84	52.05	52	7.3	2011-06-24T03:09:39
168.23	-20.24	11	6.8	2011-05-10T08:55:08
161.2	-10.38	79	6.8	2011-04-23T04:16:54
141.59	38.28	42	7.1	2011-04-07T14:32:43
144.59	38.06	19	7.7	2011-03-11T06:25:50
141.11	36.28	43	7.9	2011-03-11T06:15:40
142.37	38.3	29	9.1	2011-03-11T05:46:24
142.84	38.44	32	7.3	2011-03-09T02:45:20
-72.96	-36.42	26	6.9	2011-02-11T20:05:30
63.95	28.78	68	7.2	2011-01-18T20:23:23
-73.33	-38.35	24	7.2	2011-01-02T20:20:17
-63.14	-26.8	577	7	2011-01-01T09:56:58

167.95	-19.7	16	7.3	2010-12-25T13:16:37
143.7	26.9	14	7.4	2010-12-21T17:19:40
139.19	28.35	470	6.8	2010-11-30T03:24:40
100.08	-3.49	20	7.8	2010-10-25T14:42:22
133.76	-4.96	26	7	2010-09-29T17:11:25
171.83	-43.52	12	7	2010-09-03T16:35:47
141.47	12.49	16	6.9	2010-08-13T21:19:34
-77.31	-1.27	207	7.1	2010-08-12T11:54:15
168.07	-17.54	25	7.3	2010-08-10T05:23:44
150.76	-5.75	44	7	2010-08-04T22:01:43
123.26	6.78	641	7.5	2010-07-23T23:15:10
123.48	6.5	578	7.6	2010-07-23T22:51:11
123.41	6.72	607	7.3	2010-07-23T22:08:11
150.59	-5.93	35	7.3	2010-07-18T13:34:59
150.43	-5.97	28	6.9	2010-07-18T13:04:09
136.54	-2.17	18	7	2010-06-16T03:16:27
91.94	7.88	35	7.5	2010-06-12T19:26:50
166.64	-13.7	31	7.2	2010-05-27T17:14:46
96.02	3.75	38	7.2	2010-05-09T05:59:41
96.55	33.16	17	6.9	2010-04-13T23:49:38
161.12	-10.88	21	6.9	2010-04-11T09:40:25
97.05	2.38	31	7.8	2010-04-06T22:15:01
-71.8	-34.33	18	7	2010-03-11T14:55:27
-71.89	-34.29	11	6.9	2010-03-11T14:39:43
100.99	-3.76	26	6.8	2010-03-05T16:07:00
-75.05	-37.77	35	7.4	2010-02-27T08:01:23
-72.9	-36.12	23	8.8	2010-02-27T06:34:11
128.43	25.93	25	7	2010-02-26T20:31:26
130.7	42.59	578	6.9	2010-02-18T01:13:19
-72.57	18.44	13	7	2010-01-12T21:53:10
157.55	-9.02	15	6.8	2010-01-05T12:15:32
-14.7	-58.17	13	6.8	2010-01-05T04:55:39
157.35	-8.78	10	7.1	2010-01-03T22:36:25

Reference

Auld, B. A. (1990). *Acoustic fields and waves in solids. Vol. 1 Vol. 1*. Malabar: Krieger Publishing Company.

Chapman, C. H. (1981). Generalized Radon transforms and slant stacks. *Geophysical Journal International*, *66*(2), 445–453. https://doi.org/10.1111/j.1365-246X.1981.tb05966.x

Kennett, B. L. N., Engdahl, E. R., & Buland, R. (1995). Constraints on seismic velocities in the Earth from traveltimes. *Geophysical Journal International*, *122*(1), 108–124. https://doi.org/10.1111/j.1365-246X.1995.tb03540.x

Lin, J.-F., Mao, Z., Yavaş, H., Zhao, J., & Dubrovinsky, L. (2010). Shear wave anisotropy of textured hcp-Fe in the Earth's inner core. *Earth and Planetary Science Letters*, *298*(3), 361–366. https://doi.org/10.1016/j.epsl.2010.08.006

Mao, W. L., Struzhkin, V. V., Baron, A. Q. R., Tsutsui, S., Tommaseo, C. E., Wenk, H.-R., et al. (2008). Experimental determination of the elasticity of iron at high pressure. *Journal of Geophysical Research: Solid Earth*, *113*(B9). https://doi.org/10.1029/2007JB005229

Mattesini, M., Belonoshko, A. B., Buforn, E., Ramírez, M., Simak, S. I., Udías, A., et al. (2010). Hemispherical anisotropic patterns of the Earth's inner core. *Proceedings of the National Academy of Sciences*, *107*(21), 9507–9512. https://doi.org/10.1073/pnas.1004856107

Phạm, T.-S., Tkalčić, H., Sambridge, M., & Kennett, B. L. N. (2018). Earth's Correlation Wavefield: Late Coda Correlation. *Geophysical Research Letters*, *45*(7), 3035–3042. https://doi.org/10.1002/2018GL077244

Romanowicz, B., Cao, A., Godwal, B., Wenk, R., Ventosa, S., & Jeanloz, R. (2016). Seismic anisotropy in the Earth's innermost inner core: Testing structural models against mineral physics predictions. *Geophysical Research Letters*, *43*(1), 93–100. https://doi.org/10.1002/2015GL066734

Shearer, P. M. (1994). Constraints on inner core anisotropy from PKP(DF) travel times. *Journal of Geophysical Research: Solid Earth*, *99*(B10), 19647–19659. https://doi.org/10.1029/94JB01470

Song, X. (1997). Anisotropy of the Earth's inner core. *Reviews of Geophysics*, *35*(3), 297–313. https://doi.org/10.1029/97RG01285

Song, X., & Helmberger, D. V. (1995). Depth dependence of anisotropy of Earth's inner core. *Journal of Geophysical Research: Solid Earth*, *100*(B6), 9805–9816. https://doi.org/10.1029/95JB00244

Vočadlo, L., Dobson, D. P., & Wood, I. G. (2009). Ab initio calculations of the elasticity of hcp-Fe as a function of temperature at inner-core pressure. *Earth and Planetary Science Letters*, *288*(3), 534–538. https://doi.org/10.1016/j.epsl.2009.10.015

828 Wang, S., & Tkalčić, H. (2020). Seismic event coda-correlation's formation: implications for global seismology. *Geophysical*
829 *Journal International*, *222*(2), 1283–1294. https://doi.org/10.1093/gji/ggaa259

830
831
832
833